

REPORT DOCUMENTATION PAGE				Form Approved OMB No. 0704-0188		
<p>The public reporting burden for this collection of information is estimated to average 1 hour per response, including the time for reviewing instructions, searching existing data sources, gathering and maintaining the data needed, and completing and reviewing the collection of information. Send comments regarding this burden estimate or any other aspect of this collection of information, including suggestions for reducing the burden, to the Department of Defense, Executive Service Directorate (0704-0188). Respondents should be aware that notwithstanding any other provision of law, no person shall be subject to any penalty for failing to comply with a collection of information if it does not display a currently valid OMB control number.</p>						
PLEASE DO NOT RETURN YOUR FORM TO THE ABOVE ORGANIZATION.						
1. REPORT DATE (DD-MM-YYYY) 14-05-2013	2. REPORT TYPE Final	3. DATES COVERED (From - To) 08-15-2007 to 02/14/2013				
4. TITLE AND SUBTITLE Diode Laser Pumped Alkali Vapor Lasers with Exciplex-Assisted Absorption			5a. CONTRACT NUMBER			
			5b. GRANT NUMBER FA9550-07-1-0572			
			5c. PROGRAM ELEMENT NUMBER			
6. AUTHOR(S) Michael C. Heaven and Leonid Glebov			5d. PROJECT NUMBER			
			5e. TASK NUMBER			
			5f. WORK UNIT NUMBER			
7. PERFORMING ORGANIZATION NAME(S) AND ADDRESS(ES) Emory University, 1515 Dickey Drive, Atlanta, GA 30322 The College of Optics and Photonics, University of Central Florida, 4000 Central Florida Blvd. Orlando, Florida, 32816			8. PERFORMING ORGANIZATION REPORT NUMBER			
9. SPONSORING/MONITORING AGENCY NAME(S) AND ADDRESS(ES) Air Force Office of Scientific Research (AFOSR) 875 North Randolph Street Suite 325, Room 3112 Arlington, Virginia 22203			10. SPONSOR/MONITOR'S ACRONYM(S)			
			11. SPONSOR/MONITOR'S REPORT NUMBER(S) AFRL-AFOSR-VA-TR 2016-0692			
12. DISTRIBUTION/AVAILABILITY STATEMENT Unclassified/unlimited						
13. SUPPLEMENTARY NOTES						
14. ABSTRACT <p>Gain and lasing for optically pumped metastable Ne*, Ar*, Kr* and Xe* was demonstrated. Three-level lasing schemes were used, with He as the energy transfer agent that established the population inversion. The excitation source used in these initial studies was a pulsed optical parametric oscillator. The lasers operated at 703.2 (Ne*), 912.5 (Ar*), 893.1 (Kr*) and 980.2 nm (Xe*). Peak powers as high as 27kW/cm² were observed for Ar*. Lasing of Ar* was also demonstrated using a 7.5W CW diode laser supplied by the group at UCF. Techniques were developed for spectral narrowing of semiconductor lasers by volume Bragg gratings (VBGs) recorded in photo-thermo-refractive (PTR) glass. This technology provides efficient excitation by radiation of low pressure Rb and Cs vapors from ground states and by low pressure Ar* and Kr* from metastable states. Exposed and developed PTR glass with an absorption of 0.0006 /cm at 780 nm was demonstrated. Spectral widths were below 20 pm. The technology transferred to OptiGrate Corporation which supplies high power pumping system to AFRL.</p>						
15. SUBJECT TERMS High-power lasers, line-narrowed diode lasers, volume Bragg grating, gas phase, DPAL, hybrid lasers.						
16. SECURITY CLASSIFICATION OF: a. REPORT unclassified		b. ABSTRACT unclassified	c. THIS PAGE unclassified	17. LIMITATION OF ABSTRACT unlimited	18. NUMBER OF PAGES unlimited	19a. NAME OF RESPONSIBLE PERSON Michael C. Heaven
				19b. TELEPHONE NUMBER (Include area code) 404 727 6617		

High Power Diode Pumped Alkali Vapor Lasers and Analog Systems

High Energy Laser Multidisciplinary Research Initiative
HEL JTO MRI

Final Report

Leonid Glebov

*The High Energy Laser Center of Excellence
University of Central Florida, School of Optics/CREOL*

Michael C. Heaven
*Department of Chemistry
Emory University
Atlanta, GA 30322*

Multidisciplinary Research Initiative led by Professor Glen P. Perram, Department of Physics, Air Force Institute of Technology, Dayton, Ohio. The final report for the AFIT program has been submitted separately.

Acknowledgement of Support and Disclaimer

This material is based upon work supported by Air Force Office of Scientific Research under Contract Number FA9550-07-1-0572. Any opinions, findings and conclusions or recommendations expressed in this material are those of the author(s) and do not necessarily reflect the views of Air Force Office of Scientific Research.

Executive Summary

Techniques were developed for spectral narrowing of semiconductor lasers by volume Bragg gratings (VBGs) recorded in photo-thermo-refractive (PTR) glass. This technology provides efficient absorption of radiation by low pressure Rb and Cs vapors from ground states and by low pressure Ar* and Kr* from metastable states. The technology was transferred to OptiGrate Corporation which supplies high power pumping system to AFRL.

A technology of PTR glass with low absorption enabling operations in high power laser beams was developed. All necessary testing setups for measurements of small absorption and scattering at 780, 808, 852, and 1085 nm with sensitivity 10^{-5} cm^{-1} were designed, assembled and used for development. Absorption spectra of PTR glass were analyzed, the main sources of additional absorption were identified, and the methods for mitigation were developed. Exposed and developed PTR glass with absorption of $6 \times 10^{-4} \text{ cm}^{-1}$ at 780 nm was demonstrated.

A technology of reflecting VBGs gratings with spectral width below 20 pm, resonant wavelength fluctuations across the aperture below 5 pm, and fine spectral tunability with accuracy ± 2 pm was developed. All necessary improvements of recording and testing setups were developed and implemented. VBGs for spectral locking of individual diodes and diode bars were fabricated and used in laser systems.

Rare gas atoms (Rg) excited to the $\text{np}^5(n+1)\text{s } ^3\text{P}_2$ configuration are metastable and have spectral properties that are closely similar to those of the alkali metals. In principle, optically pumped lasers could be constructed using excitation of the $\text{np}^5(n+1)\text{p} \leftarrow \text{np}^5(n+1)\text{s}$ transitions. This approach has the advantage of using inert reagents that are gases at room temperature, with excellent potential for closed-cycle operation. Systematic studies of Rg* energy transfer kinetics were carried out in order to assess the optimal gas mixtures and pressures for optically pumped Rg* lasers. Subsequently, gain and lasing for optically pumped Ne*, Ar*, Kr* and Xe* was demonstrated. Three-level lasing schemes were used, with He as the collisional energy transfer agent that established the population inversion. The excitation source used in these initial studies was a pulsed optical parametric oscillator. The lasers operated at 703.2 (Ne*), 912.5 (Ar*), 893.1 (Kr*) and 980.2 nm (Xe*). Peak powers as high as 27kW/cm^2 were observed for Ar*.

A continuous wave (CW), line-narrowed diode laser was constructed for optical pumping of Ar*. The pump laser was centered at 811 nm, with a tuning range of 200 pm and a linewidth of 20 pm. It provided a maximum output power of 7.5W. The initial laser demonstration experiments carried out with this laser employed a pulsed electrical discharge in Ar/He mixtures to generate Ar* metastables. With focusing of the pump beam, power dependence measurements yielded a lasing threshold pump power of 3.5 W and linear power scaling from 4-7.5 W. These measurements confirm that CW optical pumping of an Ar* laser can be accomplished using a modest power level.

Publications

1. Julien Lumeau, Larissa Glebova, Leonid B. Glebov. Influence of UV-exposure on the crystallization and optical properties of photo-thermo-refractive glass. *Journal of Non-Crystalline Solids* 354 (2008) 425–430.
2. Larissa Glebova, Julien Lumeau, Mikhail Klimov, Edgar D. Zanotto, Leonid B. Glebov. Role of bromine on the thermal and optical properties of photo-thermo-refractive glass. *Journal of Non-Crystalline Solids* 354 (2008) 456–461.
3. Julien Lumeau, Larissa Glebova and Leonid B. Glebov. Evolution of Absorption Spectra in the Process of Nucleation in Photo-Thermo-Refractive Glass. *Advanced Materials Research* 39-40 (2008) 395-398.
4. G. Venus, A. Gourevitch, V. Smirnov, and L. Glebov. High Power Volume Bragg Laser Bar with 10 GHz spectral bandwidth. *Laser Source Technology for Defense and Security IV*, edited by Mark Dubinskii, Gary L. Wood. Proc. of SPIE 6952, (2008) 69520D, 1-5.
5. A. Gourevitch, G. Venus, V. Smirnov, D. A. Hostutler, and L. Glebov. Continuous wave, 30 W laser-diode bar with 10 GHz linewidth for Rb laser pumping. *Opt. Lett.* 33 (2008) 702-704.
6. A. Podvyaznyy, G. Venus, V. Smirnov, O. Mokhun, V. Koulechov, D. Hostutler, L. Glebov. 250W diode laser for low pressure Rb vapor pumping. , Proc. of SPIE 7583 (2010) High-Power Diode Laser Technology and Applications VIII, ed. M.S. Zediker. 758313, 1-6.
7. A. Podvyaznyy, G. Venus, V. Smirnov, D. Hostutler, L. Glebov. 250 W LD bar pump source with 10 GHz spectral width for rubidium vapor medium. *Laser Technology for Defense and Security VI*, edited by Mark Dubinskii, Stephen G. Post. Proc. of SPIE Vol. 7686 (2010) 76860P, 1-7.
8. Marie-Laure Brandily-Anne, Julien Lumeau, Larissa Glebova, Leonid B. Glebov. Specific absorption spectra of cerium in multicomponent silicate glasses. *J. of Non-Crystalline Solids* 356 (2010) 2337–2343.
9. Heaven, M.C., Han, J., and Kabir, H., "Collisional relaxation of the Kr(4p⁵5p) states in He, Ne, and Kr", *Proc. SPIE* Vol. 8238, 823807/1 (2012).
10. Han, J. and Heaven, M.C., "Gain and lasing of optically pumped metastable rare gas atoms", *Opt. Lett.* Vol. 37, 2157 (2012).*
11. Kabir, M.H. and Heaven, M.C., "Energy Transfer Kinetics of the np⁵(n + 1)p Excited States of Ne and Kr", *J. Phys. Chem. A* Vol. 115, 9724 (2011).
12. Han, J. and Heaven, M. C., "Gain and lasing of optically pumped metastable rare gas atoms," *Proc. SPIE* Vol. 8547, 85470Z-1 (2012)

*This work was selected as a Research Spotlight by the rapid communication journal, Optics Letters (<http://www.opticsinfobase.org/spotlight/summary.cfm?uri=ol-37-11-2157&ori>).

The Rg* laser concept was also featured by the SPIE (International society for optics and photonics) (<http://spie.org/x91156.xml?ArticleID=x91156>).

Presentations

1. Alex Gourevitch, George Venus, Vadim Smirnov and Leonid Glebov. High-power laser diodes and bars for efficient optical pumping of rubidium vapor medium. Photonics West 2008.
2. G. Venus, A. Gourevitch, V. Smirnov, and L. Glebov. High Power Volume Bragg Laser Bar with 10 GHz spectral bandwidth. DSS 2008, Conference 6952. 2008/03/17.
3. High Power Diode Pumped Alkali Vapor Lasers and Analog Systems. HEL JTO/AFOSR MRI Program. Spectral narrowing and tuning of high power laser diodes for efficient pumping of alkali vapors. DPAL workshop. Taos, NM. 2008/04/25.
4. G. Venus, A. Gourevitch, I. Divlyanskii, V. Rotar, O. Smolsky, E. Johnson, V. Smirnov, L. Glebov. High Brightness Diodes in External Bragg Resonators. Semiconductor Laser Workshop. San Jose, CA. May 9, 2008.
5. Ivan Divliansky, Vadim Smirnov, George Venus, Alex Gourevitch, Leonid Glebov. 100 W, 20 GHz high-brightness semiconductor laser system for pumping applications. Photonics West 2009.
6. Karima Chamma, Larissa Glebova, Marie-Laure Anne, Julien Lumeau, and Leonid B. Glebov. Generation and bleaching of color centers in photo-thermo-refractive glass. To XII Conference on the Physics of Non-Crystalline Solids, paper 492. Iguassu Falls, Brazil.
7. M.L. Anne, J. Lumeau, L. Glebova and L. B. Glebov. Specific absorption coefficient of cerium in multicomponent silicate glasses. To XII Conference on the Physics of Non-Crystalline Solids, Iguassu Falls, Brazil.
8. Julien Lumeau, Karima Chamma, Larissa Glebova and Leonid B. Glebov. Ultra-low absorption and laser-induced heating of volume Bragg combiners recorded in photo-thermo-refractive glass. Photonics West 2010, San Francisco, CA.
9. Alexey Podvyaznyy, George Venus, Vadim I. Smirnov, Oleksiy Mohun, Valeriy Kuleshov, David A. Hostutler, and Leonid B. Glebov. 250W diode laser for low pressure Rb vapor pumping. Photonics West 2010, San Francisco, CA.
10. Alexey Podvyaznyy, George Venus, Vadim I. Smirnov, David A. Hostutler, and Leonid B. Glebov. 250-W LD bar pump source with 10-GHz spectral width for rubidium vapor medium. DSS, Laser Technology for Defense and Security VI 7686-23.
11. Leonid Glebov. High-power high-efficiency narrow-band diode sources for pumping rarefied gases. DPAL Workshop. Albuquerque, NM. May 26-27, 2010.
12. Julien Lumeau and Leonid B. Glebov. Mechanisms of optical bleaching of silver containing particles in photo-thermo-refractive glass. International Congress on Glass, Salvador, Brazil, September 2010.
13. George Venus, Vasile Rotar, Ivan Divliansky, Boris Zhdanov1, and Leonid Glebov. 25 W Single Laser Diode for Cesium Vapor Pumping. SSDLTR, Santa Fe, NM. 2011/06/09.
14. Leonid Glebov. Increasing brightness of laser diodes and beam combining. Workshop on challenges in power scaling of high power diode laser emitters and arrays. Marina del Rey, CA. November 4, 2011.
15. Larissa Glebova, Vadim Smirnov, Julien Lumeau, George Venus, Leonid Glebov. Low losses volume Bragg gratings recorded in photo-thermo-refractive glass. Photonics West, San Francisco, CA, 2012/01/25, Paper 8257-44.

16. George Venus, K Shavitranuruk, Ivan Divliansky, Vadim Smirnov, Leonid Glebov. High power high brightness volume Bragg semiconductor lasers. High Power Semiconductor Lasers Conference. Seattle, WA. July 9-11, 2012.
17. George Venus, K Shavitranuruk, Ivan Divliansky, Vadim Smirnov, Leonid Glebov. High power high brightness volume Bragg semiconductor lasers. SPIE Defense + Security Conference, Edinburgh, United Kingdom, September 26, 2012. Paper [8547-33]
18. M. C. Heaven, Md. Humayun Kabir and J. Han. Optically pumped atomic and molecular lasers. JTO Technical Review Meeting, Albuquerque, NM Sept 28, 2009.
19. M. C. Heaven and Md. Humayun Kabir. Energy transfer kinetics of the np⁵(n+1)p excited states of Ne and Kr. SPIE Conference on Gas and Chemical Lasers and Intense Beam Applications, The Moscone Center, San Francisco CA. January 23, 2011.
20. M. C. Heaven, Md. Humayun Kabir and J. Han. Collisional processes in optically pumped atomic gas lasers. Directed Energy Professional Society Meeting, Santa Fe, MN. June 8, 2011.
21. M. C. Heaven and J. Han. Kinetics of optically pumped rare-gas atoms. SPIE Conference on Gas and Chemical Lasers and Intense Beam Applications, The Moscone Center, San Francisco CA. January 22, 2012.
22. M. C. Heaven and J. Han. Optically Pumped Atomic Lasers. King Khalid University, Department of Physics, Abha, Saudi Arabia, March 20, 2012.
23. M. C. Heaven and J. Han. Gain and lasing of optically pumped metastable rare-gas atoms. Directed Energy Professional Society, Advanced High Power Lasers and Beam Control Conference, Broomfield, CO June 12, 2012.
24. M. C. Heaven and J. Han. Population transfer in optically pumped lasers. Dynamics on Multiple Potential Energy Surfaces, Telluride Summer Research Conference, July 11, 2012.
25. M. C. Heaven. Optically Pumped Gas Phase Lasers: the Potential for High-powers with High Beam-quality. The XIX International Symposium on High-Power Laser Systems and Applications, Istanbul, Turkey. September 11, 2012.
26. M. C. Heaven and J. Han. Gain and lasing of optically pumped metastable rare-gas atoms. SPIE Security & Defense Symposium, Edinburgh, Scotland. September 26, 2012.

Student participation (UCF)

1. Derrek Drachenberg, PhD program, graduated, works at LLNL, Livermore, CA
2. Apurva Jain, PhD program, graduated, works at AVO Photonics, Horsham, PA
3. Sergey Mokhov, PhD program, graduated, works at CREOL/UCF, Orlando, FL
4. Dylan Moses, MS Program, graduated, works at Orlando area
5. Dan Ott, PhD program
6. Mark SeGall, PhD program
7. Brian Anderson, PhD program
8. Sergey Kaim , PhD program
9. Christopher Lantigua, MS Program

Post Doctoral Fellows Supported (Emory)

1. Jiande Han
2. Md. Humayun Kabir

Section A. Work performed at The High Energy Laser Center of Excellence,

University of Central Florida

Contents

- 1.1. Introduction: spectral narrowing of lasers by volume Bragg gratings
- 1.2. Photo-thermo-refractive glass and volume Bragg gratings for high power applications
- 1.3. Single diode for pumping Rb vapor
- 1.4. Laser diode bar for pumping Rb vapor
- 1.5. Multichannel pumping system for pumping Rb vapor
- 1.6. Extreme wide aperture single diodes for pumping Cs and Rb vapors
- 1.7. Single diode for pumping metastable Ar laser

1.1. Introduction: spectral narrowing of lasers by volume Bragg gratings

A high interest in a diode-pumped alkali laser (DPAL) systems direction is connected with promising directed energy industrial and military applications. That requires developing laser solutions with high power at multi-kilowatt level, high beam quality, high efficiency, and compactness. Originally chemical gas (oxygen-iodine) lasers were perused to solve this problem. But they appeared quite inconvenient in terms of their construction. A significant progress of diode-pumping devices, which has been made in last decade, dramatically increased efficiency, power and compactness of solid state lasers. These devices demonstrated multi-kilowatt regimes but they appear limited in power because of thermo-optical distortions in a solid gain medium. Finally more than 10 years ago the idea of diode-pumped alkali laser (DPAL) had received a second life due to W. Krupke¹ to substitute diode-pumped solid state gain medium with a diode pumped cell with alkali vapor. That system consolidates efficiency and power scaling of high power diode pumped solid state lasers and high beam quality of gaseous gain medium.

The most attractive feature of alkali media is their extremely high quantum efficiency (95.3% for Cs, 98.1% for Rb and 99.6% for K as compared to 76% for 1.06 μm emission of a Nd:YAG laser). Experiments with Ti:Sapphire laser pumping showed slope efficiency more than 80% for a cesium laser at the output power of 36 W². That power level is determined by limits in power of a pumping source. An efficient high power diode laser for pumping alkali vapors can significantly increase both the output power and total wall plug efficiency.

The main problem to achieve high efficiency of pumping using commercially available laser diode bars (LDBs) is that their typical spectral line width of several nanometers ($\sim 1 \text{ THz}$) does not match with absorption line of pure alkali vapors which is about 500 MHz.

There are two approaches (as it stated in²) to solve this difficult problem. The first one is to broaden the absorption line up to 1 nm by increasing a pressure of a buffer gas up to 25 atm. However that causes a number of problems in an alkali medium such as absorption cross-section reduction, higher operation temperature, chemical reaction between alkali atoms and a buffer

¹ Krupke, W., "Diode-pumped alkali lasers (DPALs): an overview," Proc. SPIE 7005, 700521 (2008).

² Zhdanov, B. V., Knize, R. J., "Progress in alkali laser development," Proc. SPIE 6874, 68740F (2008).

gas, and distortion of laser beams in high pressure atmosphere. As a result of these processes, an alkali laser total power efficiency drop occurs. Another way is to narrow LDB spectrum to match a low pressure (~1 atm) buffer gas alkali gain medium mixture absorption line-width of 10 GHz. Such narrowing can be provided by surface diffracting gratings³ or volume Bragg gratings (VBGs)⁴.

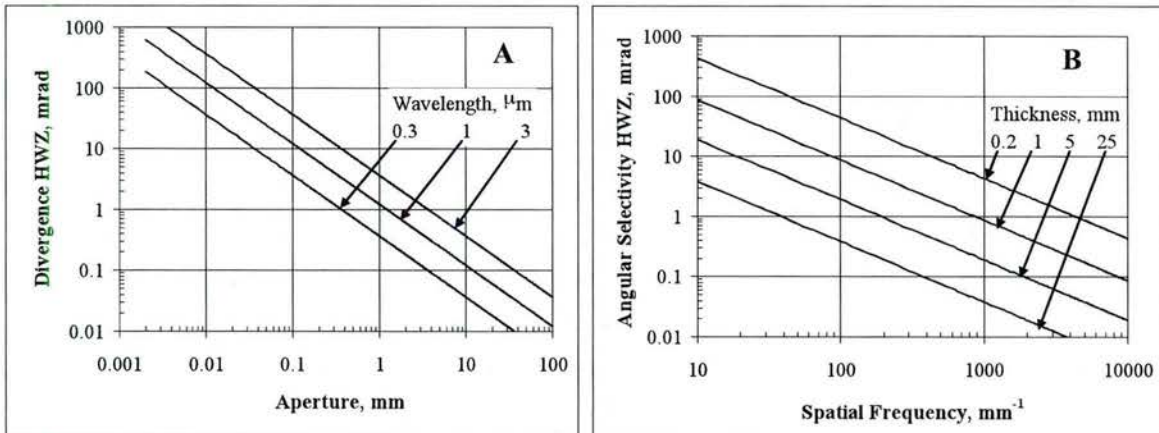


Fig. 1. Comparison of divergence of laser beams (A) and angular selectivity of Bragg gratings (B).

It is important that contrary to conventional optical elements, volume diffractive gratings are slits or apertures in space of wave vectors (or in spectral and angular spaces). This feature of thick Bragg gratings allows some unusual approaches for laser design resulting in dramatic decreasing of spectral width, conversion of wide stripe diodes to single mode emitters, and to transformation of high power semiconductor lasers to tunable sources. Such lasers that have volume Bragg gratings as the components of their resonators are called volume Bragg lasers (VOBLAs)⁵.

Figure 1 shows a comparison of diffraction limited divergence for coherent sources with different apertures and wavelengths with angular selectivity of volume Bragg gratings with different spatial frequencies and thicknesses. One can see that existing technology of PTR diffractive optical elements covers the whole region of angles from tens of degrees for narrow-stripe semiconductor lasers to tens on microradians for large aperture solid state lasers. The basic difference between a conventional design of laser resonators with mirrors, lenses and apertures versus the use of volume Bragg gratings is that the conventional elements work in geometrical space while volume gratings work directly in angular space (or space of wave vectors). This means that mode selection can be based on their different angular distribution while conventional design could produce this selection based on different spatial distribution. The use of volume Bragg gratings with properly adjusted angular and spectral selectivity as elements of laser

³ Zhdanov, B. V., Ehrenreich, T. and Knize, R.J. "Narrowband external cavity laser diode array," Electronics Letters, 43 (4), pp 221-222 (2007).

⁴ Gourevitch, A., Venus, G., Smirnov, V., and Glebov, L., "Efficient pumping of Rb vapor by high-power volume Bragg diode laser," Opt. Lett., 32 (17), pp. 2611-2613 (2007).

⁵ Leonid B. Glebov. High brightness laser design based on volume Bragg gratings. In Laser Source and System Technology for Defense and Security II, edited by Gary L. Wood, Mark A. Dubinskii, Proc. of SPIE 6216 (2006) 621601.

resonators allows selecting of arbitrary modes if they have different angular distribution independently of possible total overlapping in geometrical space.

It is important to elucidate this new feature of thick Bragg gratings for design of single transverse mode resonators. Well-known requirement for a single mode oscillation is a necessity of such aspect ratio of a resonator which results in one Fresnel zone at an output mirror. However, the feature of volume Bragg gratings to provide selection in angular space enables a new opportunity to replace this requirement by another one. This new requirement is following. Angular acceptance of output coupling device should provide propagation of radiation within the first Fresnel zone only. This requirement could be satisfied by a proper choice of thickness, spatial frequency and refractive index modulation of Bragg grating. The most important consequence of this new approach is that no restrictions for aperture of the resonator appeared. This means that a proper choice of grating can convert a wide aperture resonator with small aspect ratio to a single mode one. This feature enables increasing of power and decreasing of size for single mode lasers with divergence close to the diffraction limit.

Figure 2 shows a comparison of longitudinal mode separation in typical resonators of laser diodes and spectral width of Bragg mirrors. One can see that Bragg mirror with thickness of few of millimeters provides spectral selection enough for single longitudinal mode selection in a resonator of one or couple of millimeters length. Thus, a combination of transmitting and reflecting volume Bragg gratings provides an opportunity to select both transverse and longitudinal modes in semiconductor laser resonators.

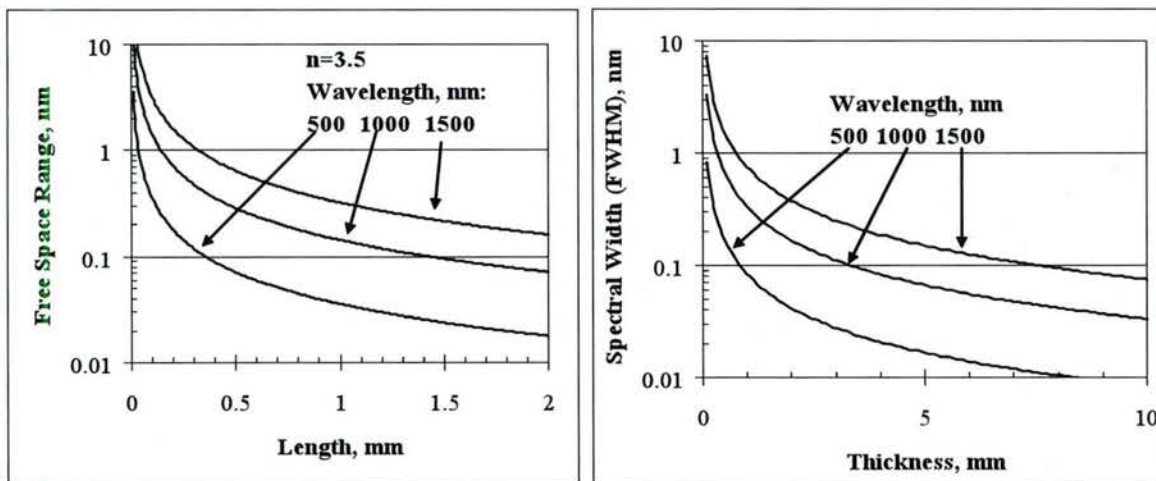


Fig. 2. Distance between longitudinal modes in Fabri-Perot resonator (A) and spectral width of volume Bragg gratings (B).

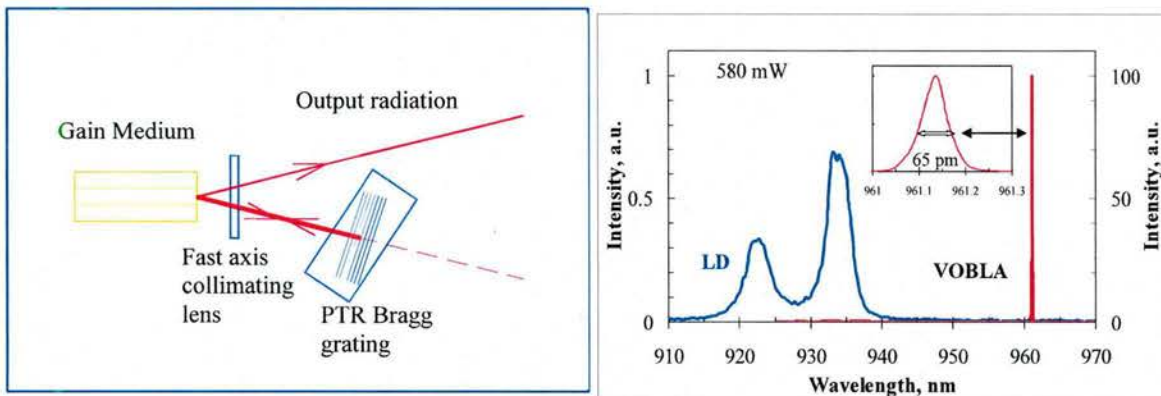


Fig. 3. Setup for spectral locking of laser diode (left) and emission spectra of an original laser diode and a volume Bragg laser consisting of the same diode and reflecting PTR grating (right).

We studied a number of volume Bragg lasers with different LDs having stripe widths from 30 to 250 μm and reflection from the front facet from 0.5 to 5% combined with PTR Bragg gratings having reflection coefficients from 3 to 99% and spectral widths from 1 nm to 100 pm⁶. It was found that any type of laser diode can be locked practically by any of tested gratings if its central wavelength is not away from a maximum of a diode emission spectrum for more than several nanometers. The typical example of spectral locking of a wide stripe laser diode is shown in Fig. 3. One can see that while a bare LD has a wide emission spectrum of several nanometers, a volume Bragg laser can have wavelength outside of this spectral region because of very wide luminescence bands of semiconductors. It is important that for bare diode emission line has a thermal shift of about 0.3 nm/K, while VOBLA has narrow emission band which is completely locked by a PTR Bragg grating. Spectral width of the emission band can be easily narrower to the range of tens of picometers. Total losses in this case do not exceed 3% while spectral brightness increases for almost two orders of magnitude. The ranges of pumping current, temperature variation or spectral detuning are wider if reflection coefficient from front facet is lower, length of a diode is shorter, and reflection coefficient of Bragg mirror is higher.

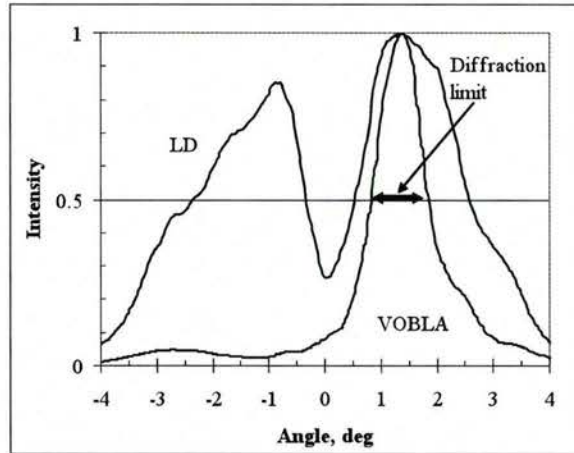


Fig. 4. Divergence of an original laser diode and a volume Bragg laser consisting of the same diode and reflecting PTR grating.

⁶ G.B. Venus, A. Sevian, V.I. Smirnov, L.B. Glebov, "High-brightness narrow-line laser diode source with volume Bragg-grating feedback" High-Power Diode Laser Technology and Applications III, edited by Mark S. Zediker, Proc. of SPIE 5711 (2005) 166-176.

Selection of a single transverse mode in VOBLA is possible if angular divergence of a particular mode is adjusted with angular acceptance of Bragg grating used in the resonator. The result of the use of reflecting PTR Bragg grating is shown in Fig. 4. One can see that external resonator with reflecting PTR Bragg grating provides angular selectivity of output radiation close to the diffraction limit even at high levels of pumping exceeding threshold for more than 10 times. Single transverse mode emission from a wide stripe laser diodes were obtained for stripe widths up to 250 μm with total power of 2 W in a beam with diffraction limited divergence. This approach can be applied for different types of lasers providing diffraction limited divergence for resonators having high Fresnel numbers. Thus, the use of a properly adjusted PTR Bragg grating as an output coupler of an external resonator allows single mode operation for wide stripe semiconductor laser diodes at high levels of pumping.

1.2. Photo-thermo-refractive glass and volume Bragg gratings for high power applications

The improvements towards decreasing of the losses of volume Bragg gratings (VBG's) in PTR glass at 780 and 852 nm requires being able to perform separate measurements of scattering and absorption at these wavelengths. We focused our attention on the design and assembly of a specific setup that will allow measuring of low-level absorption and scattering at 780 and 852 nm (Fig. 5). The setup is based on a combination of several measurement techniques in a single run of experiments. This setup provides photometric measurement of transmitted and reflected power with accuracy about 0.1%. Low absorption measurements are provided by heating of a sample and evaluation of its temperature by measurements of its emission in mid IR region delivered to a photodetector by an IR transparent fiber. Additional modification of this setup was based on a pump/probe configuration (Fig. 6). A probe beam (He-Ne laser) is sent at normal incidence through the volume Bragg grating in PTR glass that has to be characterized. When He-Ne beam is passing through the VBG sample, multiple reflections at each interface result in the appearance of multi-waves Fabry-Perot interference. The intensity of the signal at the output of the sample is then proportional to its optical thickness. The second laser, which is overlapped with the probe beam, is used to pump the glass. In the presence of absorption, a part of this radiation is absorbed and converted into heat. It results in a change of the optical thickness of the sample which is proportional to the absorbed power. This modification enabled low absorption measurements not only in specially prepared sample but directly in VBGs fabricated for high power applications.

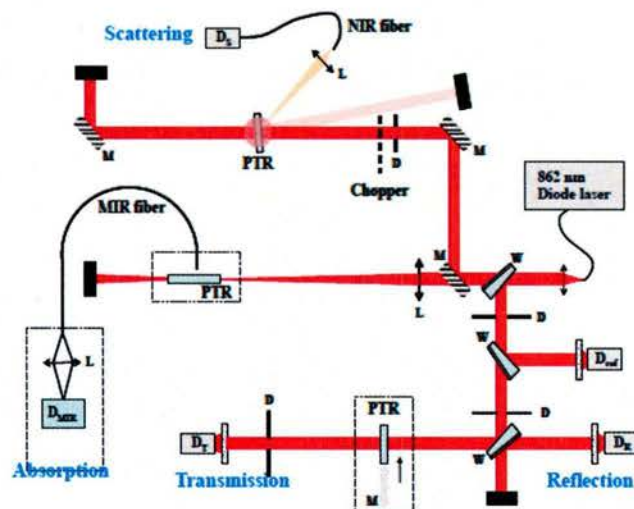


Fig. 5. Experimental setup for small absorption, reflection and scattering measurements at 780, 852 and 1064 nm.

Additional modification of this setup was based on a pump/probe configuration (Fig. 6). A probe beam (He-Ne laser) is sent at normal incidence through the volume Bragg grating in PTR glass that has to be characterized. When He-Ne beam is passing through the VBG sample, multiple reflections at each interface result in the appearance of multi-waves Fabry-Perot interference. The intensity of the signal at the output of the sample is then proportional to its optical thickness. The second laser, which is overlapped with the probe beam, is used to pump the glass. In the presence of absorption, a part of this radiation is absorbed and converted into heat. It results in a change of the optical thickness of the sample which is proportional to the absorbed power. This modification enabled low absorption measurements not only in specially prepared sample but directly in VBGs fabricated for high power applications.

Using this technique and a calibrated reference sample, it is therefore possible to perform a measurement of the absorption with high precision. In order to carry out measurement of absorption at 780 nm, we used a laser diode bar combined with a projection lens which projected a ~4 mm square aperture at the front surface of the sample.

Maximum output power of the bar was equal to 20 W and such power was enough to allow measurement of absorption below levels of 10^{-4} cm^{-1} in a 1-mm-thick sample.

Normal processing of PTR glass includes its exposure to ionizing UV radiation and then thermal treatment. In order to study the structure of absorption in UV-exposed and thermally developed PTR glass we measured and analyzed spectra of losses which are a sum of absorption and

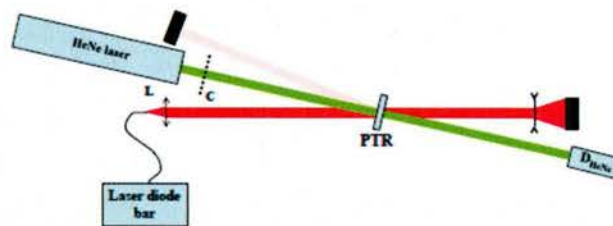


Fig. 6. Experimental setup for laser interferometry at 780, 808 and 852 nm in glass plates and in volume gratings. L: lens; C: chopper; D: detector and acquisition system.

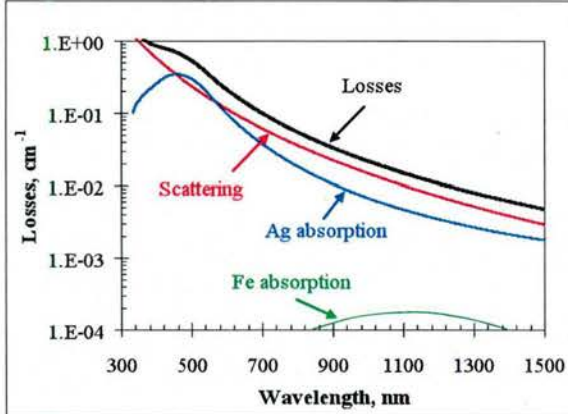


Fig. 7. Absorption spectrum of UV-exposed and thermally developed PTR glass and its decomposition into scattering and absorption components.

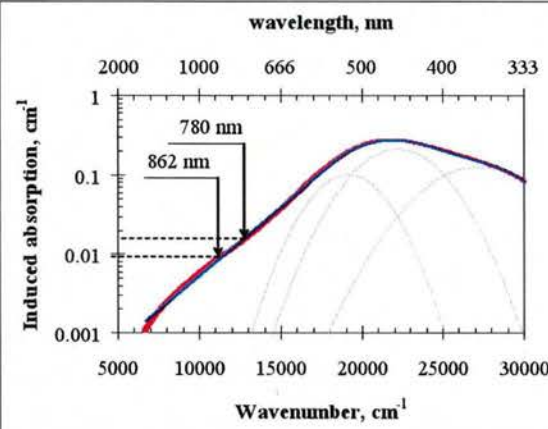


Fig. 8. Absorption spectrum of silver bromide particles in UV-exposed and thermally developed PTR glass and its decomposition to Gaussian bands.

scattering (Fig. 7). We decomposed this losses spectrum into several contributions. One can see that the main type of losses is scattering. Regarding absorption, the main absorption is due to the silver containing particles. It is shown in Fig. 8 that the absorption band of silver containing particles is actually the sum of the absorption bands of hole centers, colloidal silver particles, colloidal silver bromide particles and complex colloidal silver/silver bromide particles⁷. The last two have long-wavelength Urbach tails which extends to 1.5 μm regions and therefore, they have very important impact on the absorption in 700-900 nm region. Precise measurement using the

⁷ J. Lumeau, L. Glebova and L.B. Glebov, "Investigation of the induced absorption and scattering in visible and NIR ranges in photo-thermo-refractive glass", *International Congress on Glass* (Strasbourg, France), paper M3, July 2007

interferometric setup showed that this absorption is in the order of 10^{-2} cm^{-1} and therefore incompatible with any high power applications.

In order to mitigate these absorption, it was shown that the absorption of silver containing particles can be partially optically bleached using the second harmonic of a Nd:YAG laser. We developed and optimized a method for optical bleaching that enabled significant decrease of absorption below 10^{-3} cm^{-1} at 852 and 1085 nm (Fig. 9). Such level of absorption corresponds to the almost complete bleaching of the silver containing particles and returns the absorption to the level of absorption similar to the one measured in virgin glasses.

To enable the use of VBGs in high power pumping systems, we conducted comprehensive modeling of thermal distortions produced by VBGs for diffracted and transmitted beams. Figure 10 shows the result of such a modeling. Model parameters: laser power – 1 kW, absorption

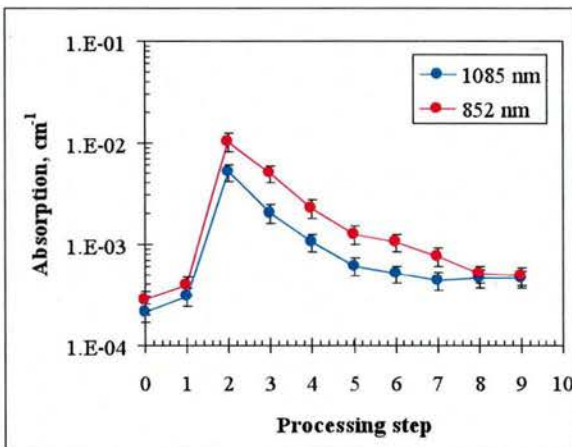


Fig. 9. Evolution of the absorption at 852 and 1085 nm in UV-exposed and thermally developed PTR glass during the bleaching process.

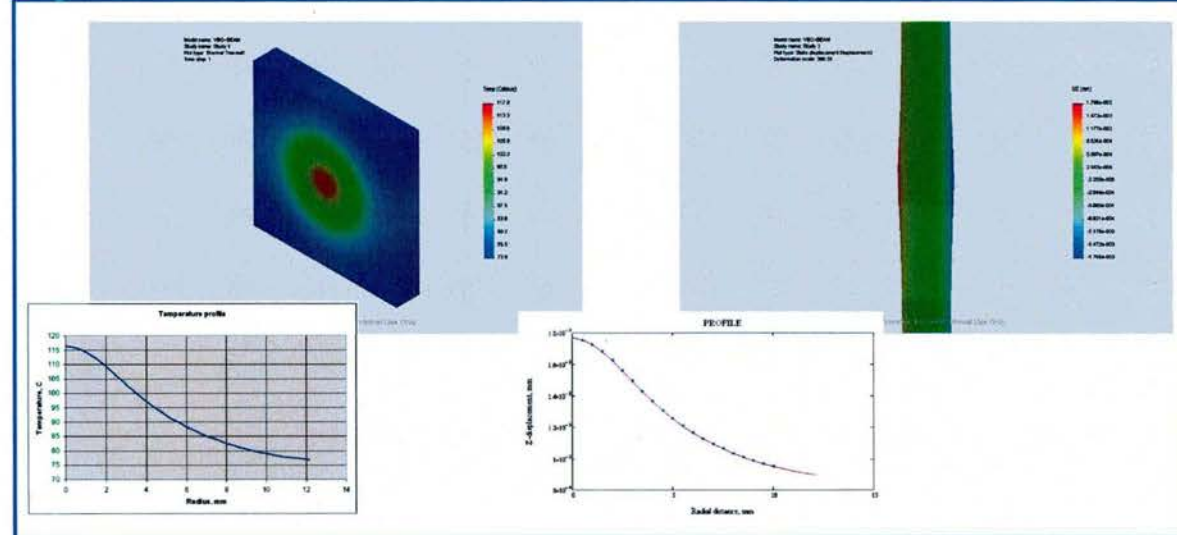


Fig. 10. Modeling of thermal distortions in Volume Bragg Grating exposed to high power laser radiation.

coefficient - 10^{-3} cm^{-1} , VBG size $25 \times 25 \times 4 \text{ mm}^3$, beam diameter - 7mm, free air convection in room temperature. Thermal lens is about 20 m focal length. This result shows that for pumping systems with the use of laser diode bars, a current technology of VBGs recorded in PTR glass enables operations with no forced cooling. However, precise positioning of Bragg wavelength would require thermal control of VBGs that will be described later.

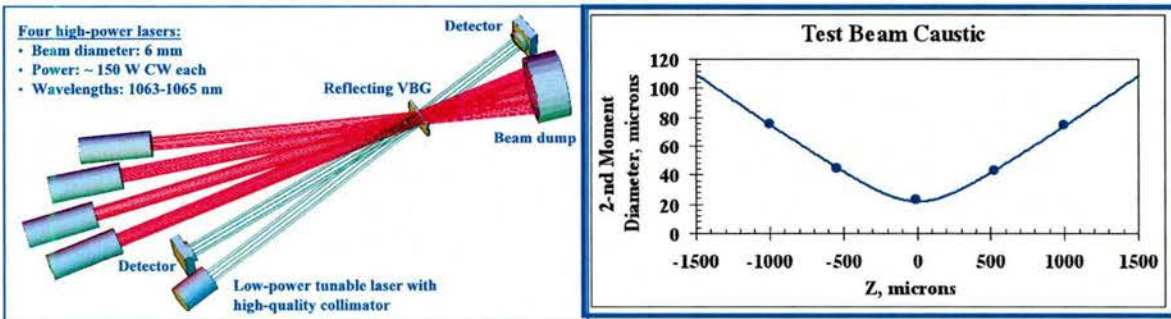


Fig. 11. Experimental setup for testing VBGs in high power laser beams (left) and beam quality (right) of a probe beam ($M^2=1.1$) diffracted from a grating illuminated with 770 W and power density of 2.75 kW/cm^2 .

To confirm the results of modeling, a VBG was tested in maximum available power laser beam (Fig. 11). Four laser beams with total power of 770 W (power density 2.75 kW/cm^2) were launched to a VBG. A probe beam produced by a single mode tunable laser was diffracted by the VBG and diffraction efficiency and beam quality of the diffracted beam were measured. It was found that diffraction efficiency is not deteriorated at this power level. Thermal shift of Bragg wavelength at 780 nm is about 8 nm/K. Quality of the diffracted beam was close to the diffraction limit ($M^2=1.1$).

Modeling of VBGs based on coupled waves theory gas shown that necessary spectral width of 20 pm could be achieved in PTR glass with thickness of 17 mm. Such thick holographic mirror is a challenge because of extremely high requirements for optical quality of used PTR glass plate, low level of aberrations in a recording beam, and high uniformity of thermal field in a development furnace. All those tasks were successfully solved and VBGs operating at 780 and 852 nm were successfully recorded (Fig. 12). This technology was transferred to OptiGrate Corp. that produced such gratings for all required pumping systems used at AFRL.

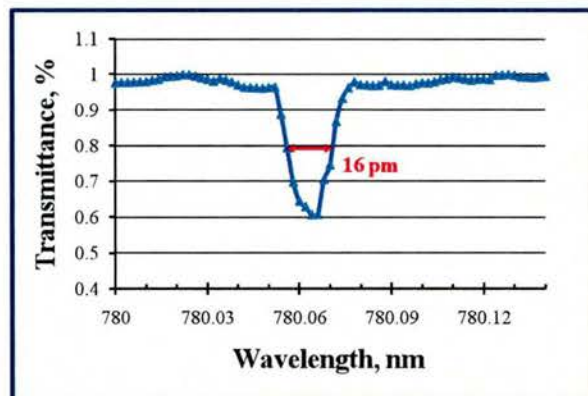


Fig. 12. Transmission spectrum of a 17 mm thick VBG for spectral locking of a laser diode bar.

1.3. Single diode for pumping Rb vapor

The volume Bragg laser (VOBLA) consisted of an off-shelf LD, a fast-axis collimator and a reflective volume Bragg grating as a wavelength selective output coupler. The 17-mm-thick reflecting Bragg grating (RBG) in a PTR glass was specially designed and fabricated at OptGrate. This mirror with $5 \times 6 \text{ mm}^2$ aperture had 70% diffraction efficiency for plane wave, 30 pm (15 GHz) spectral selectivity (FWHM), and 1° angular selectivity (FWHM). The resonant Bragg wavelength of the RBG at normal incidence (retro-reflection) was 779.92 nm corresponding to refractive index modulation period of 0.26 μm . The RBG and a fast axis collimator had antireflection coatings to prevent the parasitic reflections. The LD and RBG were mounted on thermoelectrically cooled copper heatsinks with temperature stability of $\pm 0.01 \text{ K}$.

The laser spectral characteristics were studied in CW operation. To evaluate the overall emission spectra of free-running LD and VOBLA, the laser output radiation was collected into an integrating sphere and then was coupled into an optical spectrum analyzer (OSA) using a single mode fiber. The spectral resolution of the experimental setup was 15 GHz (30 pm). The laser spectral width and mode structure were initially evaluated using Fabry-Perot etalon with 15 GHz free spectrum range and 0.8 GHz spectral resolution. The precise measurement of VOBLA mode structure was performed using scanning confocal Fabry-Perot interferometer with 10 GHz free spectrum range and 67 MHz spectral resolution.

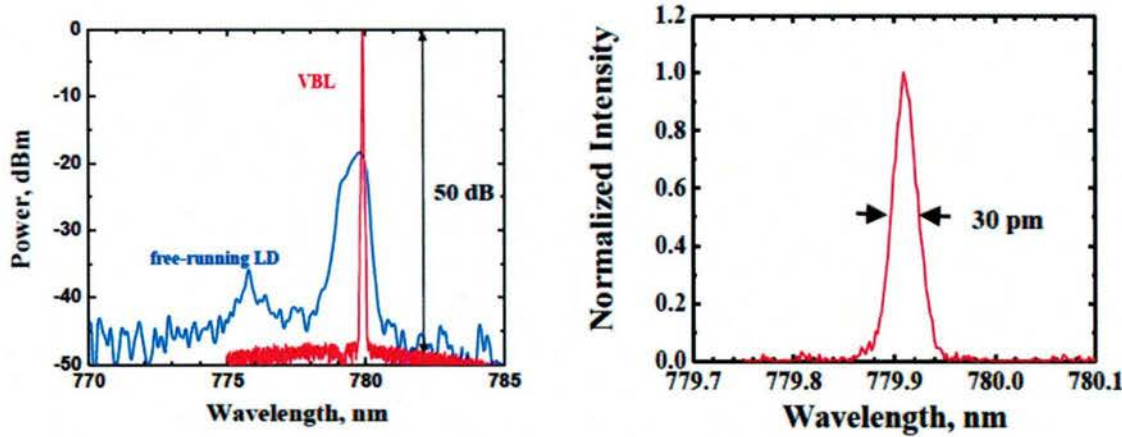


Fig. 13. Emission spectra of free-running (blue line) and volume Bragg (red line) diode lasers in semi-log scale (left) and emission spectrum of a volume Bragg laser in linear scale (right).

Figure 13 shows the emission spectra of free running (blue line) and volume Bragg (red line) diode lasers measured at 1-W CW output power. The temperatures of LD and RBG were 18 and 25°C, respectively. The emission spectrum of a free-running LD had maximum around 780 nm and spectral width of 2 nm (FWHM). The emission spectrum of VOBLA was narrowed into 30 pm FWHM which corresponded to spectral resolution of the OSA. The side mode suppression ratio was better than 45 dB. The VOBLA spectral linewidth was evaluated by measuring the emission spectrum using Fabry-Perot etalon with free spectrum range overlapping with spectral resolution of OSA. It was determined that the VOBLA linewidth did not exceed 7 GHz.

The detailed mode structure of VOBLA was measured by scanning confocal Fabry-Perot interferometer. Figure 14 shows mode structure of VOBLA outputting 1 W CW power. The external cavity resonator supported up-to four modes with ~ 2 GHz mode spacing and 7 GHz spectral bandwidth. This mode spacing is in good agreement with estimated distance between adjacent longitudinal modes in the given external resonator. Typically, more than 80% of emitting power was concentrated within one or two of those modes.

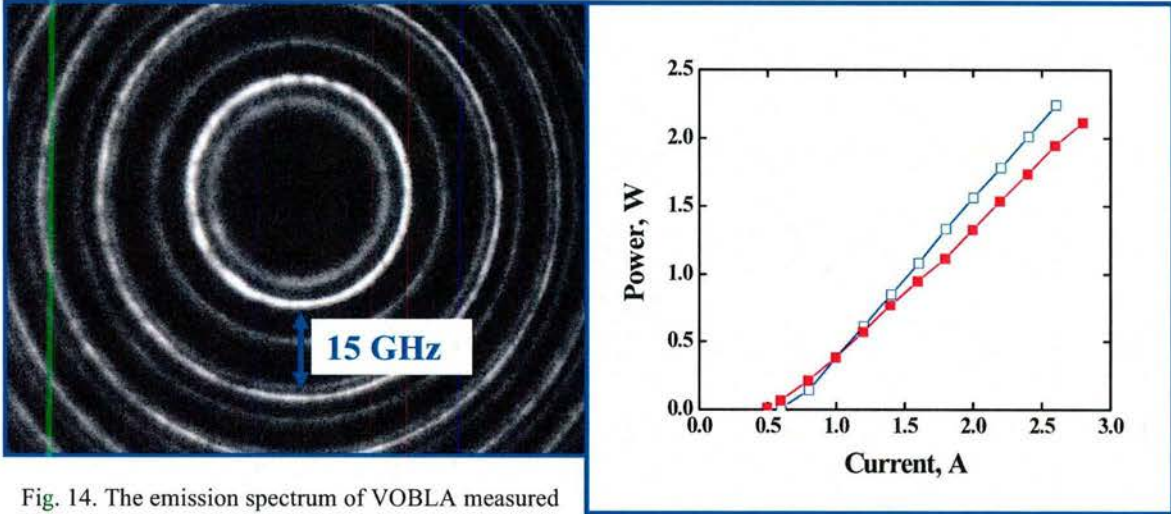


Fig. 14. The emission spectrum of VOBLA measured by a scanning confocal Fabry-Perot interferometer with 15 GHz free spectral range.

Fig. 15. Output CW power of a free-running (hollow square) and volume Bragg (solid square) diode lasers vs driving current.

Figure 15 shows that dramatic spectral narrowing into 7 GHz linewidth leads to only $\sim 10\%$ decrease of output power. The current threshold decrease and slope efficiency drop are resulted from higher reflection from external Bragg mirror in comparison with the free running LD. To evaluate this result we estimated the VBG reflectivity for the incident divergent beam. The far-field pattern of the free-running LD was measured along slow-axis. The FWHM of the far-field pattern was about 7° comparing with 1° angular selectivity of RBG. So only the seventh part of the LD beam was reflected back by the given VBG which had 70% reflectivity for the plane wave. The VBG reflectivity can be roughly estimated as 10% for the incident LD beam that is in a good agreement with the estimation of LD output mirror reflectivity.

The optical pumping of rubidium vapor mediums requires the pumping laser tunability to reach the precise overlapping between Rb absorption bands and the pumping laser emission spectrum. The VOBLA emission spectrum was thermally tuned over 300 pm spectral range by heating RBG which provided thermal shift of Bragg wavelength with rate of 8 pm/K (Fig. 16). The thermal shift of wavelength does not deteriorate the laser spectrum width.

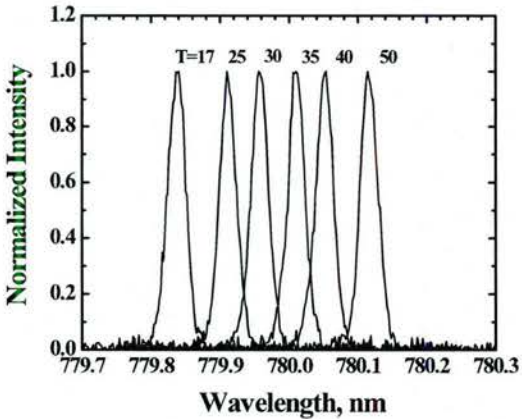


Fig. 16. The emission spectra of a volume Bragg diode laser at different grating temperatures.

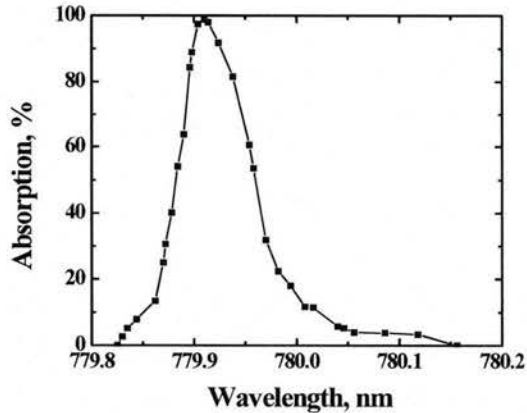


Fig. 17. Absorption of volume Bragg laser radiation by a Rb cell vs. central wavelength of emission.

The absorption of the pump light by Rb atoms was measured in Rb cell at 420 K. The cell contained Rb vapor mixed with C₂H₆ buffer gas. The buffer gas pressure was 300 Torr (0.4 Atm). Such conditions did not significantly contribute into Doppler and collision broadening mechanisms of Rb absorption spectrum. Figure 17 shows absorption of laser radiation by the Rb cell versus central wavelength of VOBLA. The central wavelength was determined as the average weighted wavelength of an emission spectrum recorded by OSA. The low-pressure Rb cell absorbed more than 95% of VOBLA radiation at wavelength of 779.92 nm.

The diode laser at 780 nm with volume Bragg grating as an output coupler has demonstrated CW power up to 2 W with slope efficiency of 1 W/A, spectral width (FWHM) of 7 GHz (14 pm), and tunability over 300 pm. More than 95% laser intensity was absorbed by the Rb cell mixed with low-pressure C₂H₆ buffer gas.

1.4. Laser diode bar for pumping Rb vapor

In this section, we report on the development of a volume Bragg laser (VOBLA) operating at 780 nm with a 30-W CW output power. The VOBLA output power is 90% of the free running LDB power. The VOBLA emission spectrum width was on the order of 10 GHz (FWHM), the spectral contrast was about 40 dB, and the laser radiation absorption by a low pressure Rb-cell at 780 nm was 90%.

The VOBLA consisted of an off-the-shelf passively cooled LDB, a fast-axis collimator and a reflective volume Bragg grating using as a wavelength selective output coupler. The LDB was fabricated by LaserTel Inc. and consisted of 24 LDs with 2 mm cavity length and 150 μ m aperture width. The LDs were equally distributed across the 1-cm-wide LDB. The 18-mm-thick Bragg mirror was designed and fabricated at OptiGrate. This mirror had a diffraction efficiency of 70% for the plane wave at the resonant wavelength. The spectral and angular selectivity of the mirror were around 30 pm and 1° (FWHM), respectively. The resonant Bragg wavelength at normal incidence (retro-reflection) was measured to be 779.7 nm. The resonant Bragg wavelength uniformity was better than 10 pm across the 5×15 mm² aperture. The fluctuation of

diffraction efficiency was less than 5% across the full aperture. The Bragg mirror and a fast axis collimator had antireflection coatings to prevent parasitic reflections. The LDB and Bragg mirror were mounted on thermoelectrically cooled copper heat-sinks with a temperature stability of ± 0.1 K.

The free-running LDB and VOBLA were studied in CW operation. To evaluate the overall laser emission spectra, the output radiation was collected into an integrating sphere and was coupled into an optical spectrum analyzer (OSA) (ANDO AQ6317B) using a single-mode fiber. The spectral resolution of the experimental setup was 15 GHz (30 pm). The precise measurement of the VOBLA mode structure and spectral width was performed using an experimental Fabry-Perot interferometer with 15 GHz free spectrum range (FSR) and 0.8 GHz spectral resolution.

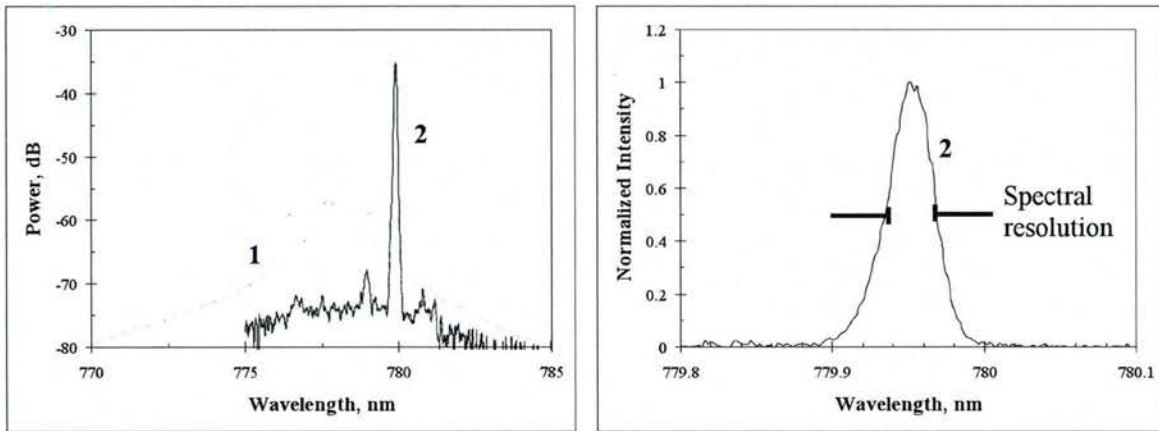


Fig. 18. Emission spectra of free-running (1) and volume Bragg (2) diode laser bars measured by an optical spectrum analyzer with resolution of 30 pm.

Figure 18 shows the emission spectra of the free running (dotted line) and volume Bragg (solid line) laser diode bars measured at 20 W CW output power. The emission spectrum of the free-running LDB had a maximum around 780 nm and a spectral width of 5 nm (FWHM) at room temperature. After integration of the LDB into the external Bragg resonator, the laser emission spectrum had been narrowed down to less than 15 GHz (30 pm) (FWHM) which was the spectral resolution of the OSA. The spectral contrast (side mode suppression ratio) of VOBLA emission spectrum was approximately 40 dB. The precise value of VOBLA spectral linewidth was determined using a Fabry-Perot interferometer with 15 GHz free spectrum range. Figure 19 shows the mode structure of the VOBLA producing 20 W CW power. The spacing between next

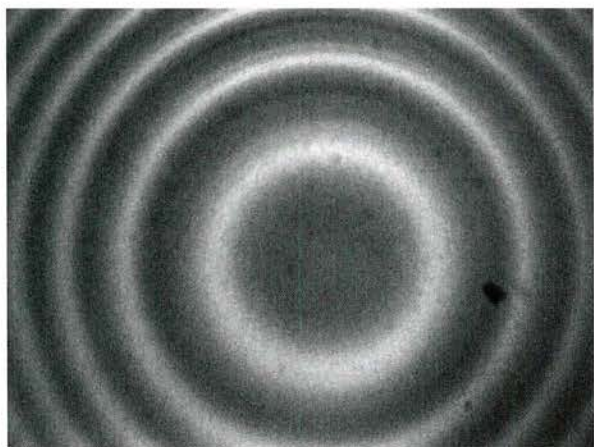


Fig. 19. The emission spectrum of the volume Bragg laser measured by Fabry-Perot interferometer with 15 GHz free spectral range.

order modes in the circular Fabry–Perot fringe pattern equals to the free spectral range (15 GHz) of the Fabry Perot interferometer. The spectral modes of individual lasers in the laser bar were overlapped producing a VOBLA spectrum with a linewidth of less than 10 GHz (FWHM). The spectral linewidth of individual LDs implemented into the similar external Bragg resonator achieved 14 pm (7 GHz). In the LDB, the emission spectra of individual LDs were slightly different due to spatial fluctuations of resonant Bragg wavelength across the aperture. The VOBLA spatial mode distribution measured at 20 W CW output power showed multimode operation with a far-field divergence of around 8° FWHM along the slow axis direction.

Compared to the free-running LDB the spectral width of the VOBLA was narrowed by 250 times with only a 10% output power decrease at maximum drive current (Fig. 20). The decrease in current threshold and drop in slope efficiency resulted from the higher reflection from the external Bragg mirror as compared to the free running LDB.

Optical pumping of rubidium vapor media requires tuning of pump laser emission to precisely overlap with Rb absorption bands. The VOBLA emission spectrum was thermally tuned over 400 pm spectral range by heating the Bragg mirror which had a thermal shift of 8 pm/K. It is important that the thermal shift of the wavelength does not increase the width of the laser spectrum. The absorption of the pump light by Rb atoms was measured in the 25-mm-thick alkali cell at 420 K. The cell contained excess Rb with a vapor phase number density of 7.2×10^{13} at/cc at 420 K mixed with C₂H₆ buffer gas (300 Torr at 298 K). This resulted in an absorption transition on the order of 8 GHz (FWHM). The Rb cell absorbed 90% of VOBLA radiation at wavelength of 779.92 nm.

Thus, a diode laser bar with a volume Bragg output coupler emitting at 780 nm produced up to 30 W CW output power with a slope efficiency of 0.8 W/A. The laser had a spectral width (FWHM) of 10 GHz (20 pm) and a tunability of over 400 pm. The output power of the volume Bragg laser exceeded 90% of the output power of the free-running laser diode bar. The low-pressure Rb cell absorbed 90% of the laser emission.

1.5. Multichannel pumping system for pumping Rb vapor

Spectrally locked laser diode bar described in the previous section was used to design a compact module. Eventually a single module can be considered as an independent laser unit performed in an individual case (Fig. 21) requiring a power supply and a heat dissipation system. Maximum emission power of this module is 35 W. At the same time the output spectrum line-width is less

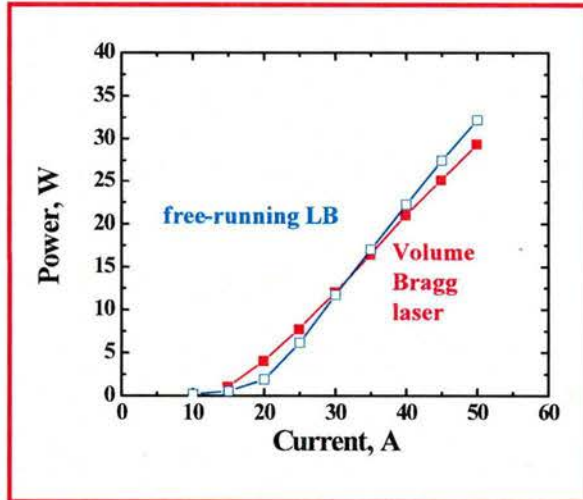


Fig. 20. CW output power of a free-running (blue line) and a volume Bragg (red line) diode laser bars versus driving current.

than 18 pm at the wavelengths of all commercially available laser diode devices. Side lobes suppression ratio is more than 30 dB. Moreover, this module provides spectral line tuning within the range of 300 pm.

The first laser system incorporates 7 modules (Fig. 22). All of the modules are tuned to the same wavelength. The output emission has a linewidth of 10 GHz and central wavelength stability within 5 pm that is sufficient to provide more than 90% absorption in low pressure Rb-gain medium. Also the system was supplied with an electronics rack containing a LDBs power source, a thermal management system and a water chiller for heat dissipation. The output emission of all the modules is coupled to a fiber bundle. The laser provides central wavelength tuning within 140 pm range. The general appearance of the laser is shown in Fig. 23.

Spectral narrowing of laser emission is shown in Fig. 24. One can see an emission spectrum of a free running 50 W LDB used for the module (blue) and the spectrum of a LDB locked in a VBG external resonator (red). Spectral width of the module is 10 GHz (FWHM), spectral contrast is above 30 dB, spectral brightness increased by 33 times, 94 % of total spectral narrowed emission power is collected within specified spectral range and slope efficiency of a narrowed module is about 90% of that for a bare LDB. A Fabry-Perot interferometer was used to measure spectral width of laser radiation. A free spectral range and a resolution were 76 pm (37.45 GHz @ 780 nm) and 2 pm respectively. A linewidth of a volume Bragg laser module was measured as 18 ± 1 pm (9.3 ± 0.5 GHz @ 780 nm) (FWHM).

The module provides spectral tuning of central wavelength by changing VBG temperature. The spectral line shape as well as its FWHM is the same within the whole tuning range. Central wavelength shift linearly depends on temperature of a VBG with a rate of 7.49 pm/K. Additional feedback provided by an external Bragg mirror results in decreasing of the threshold and slope efficiency. It is possible to increase slope efficiency of such a module

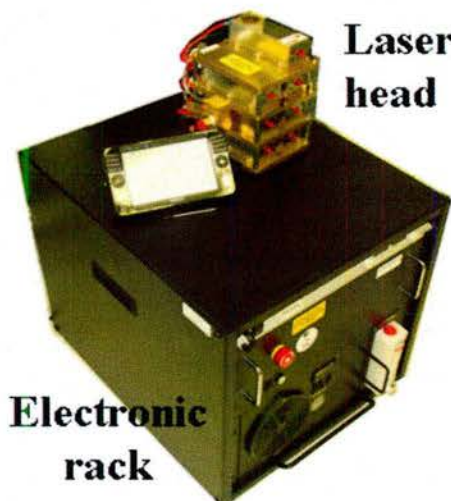


Fig. 23. General view of the 250 W laser system operating at 780 nm with 20 nm spectral width.



Fig. 21. General view of a volume Bragg laser module operating at 780 nm.

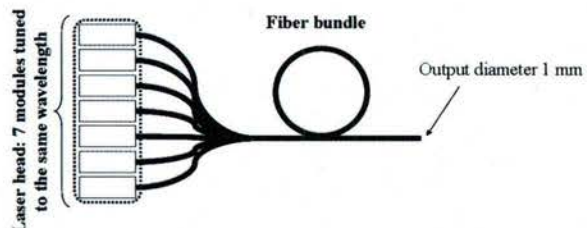


Fig. 22. Basic design of a fiber coupled laser head with a delivery fiber bundle.

by decreasing of reflection coefficient of a front facet of a laser diode. However, it would dramatically increase the cost of the laser. Therefore we made the whole system based on commercially available laser diodes.

Seven modules outputs are combined together with a fiber bundle. Special software was developed to provide a thermal control of all modules. Thus all modules were automatically tuned to the same wavelength and the whole system provided tunability within a 140 pm range. The Rb D₂ line (which is used to pump Rb DPAL) wavelength (780.033 nm) was approximately in the middle of the tunability range. For output power of 230 W, spectral width was of 19 pm (FWHM) and spectral contrast was of 23 dB (Fig. 25).

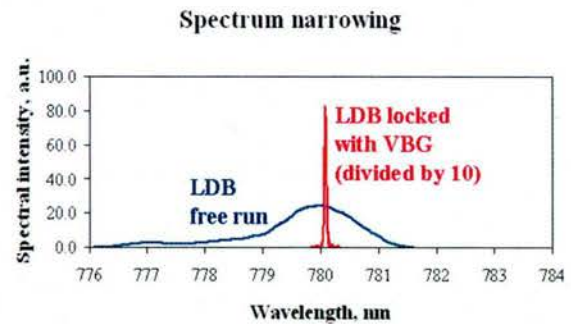


Fig. 24. Emission spectra of LD bar and volume Bragg laser module.

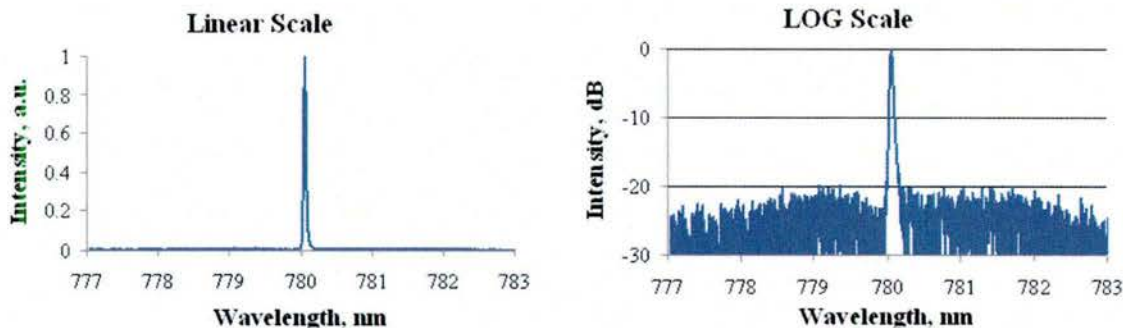


Fig. 25. Emission spectrum of a 7-module laser system operating at 200 W output power.

To test accuracy of matching of an output emission spectrum with an absorption line of low pressure Rb vapor and efficiency of pumping of a typical low pressure DPAL cell, a special setup was assembled (Fig. 26). Here an output fiber bundle of the laser head was aimed to an integrating sphere. About 0.1 % of total power was directed through a Rb-cell to a photodetector. A Rb cell (25 mm in diameter and 30 mm length) were placed in an oven providing working temperature of 120°C. The spectral position of the laser emission line was measured by an optical spectrum analyzer and absorption was measures by ratio of power after and before the cell. One can see (Fig. 26) that more than 90 % of radiation from a laser module is absorbed by a low pressure Rb-cell.

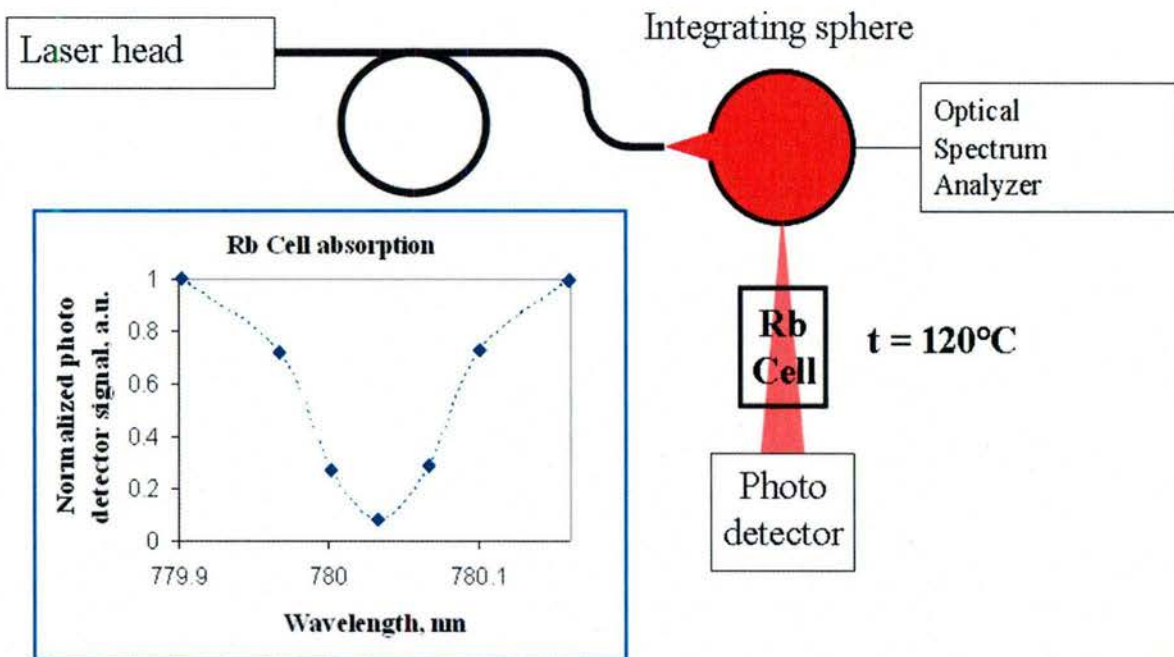


Fig. 26. Experimental setup to measure absorption of laser radiation in a Rb cell and dependence of cell transmittance on wavelength of a volume Bragg laser.

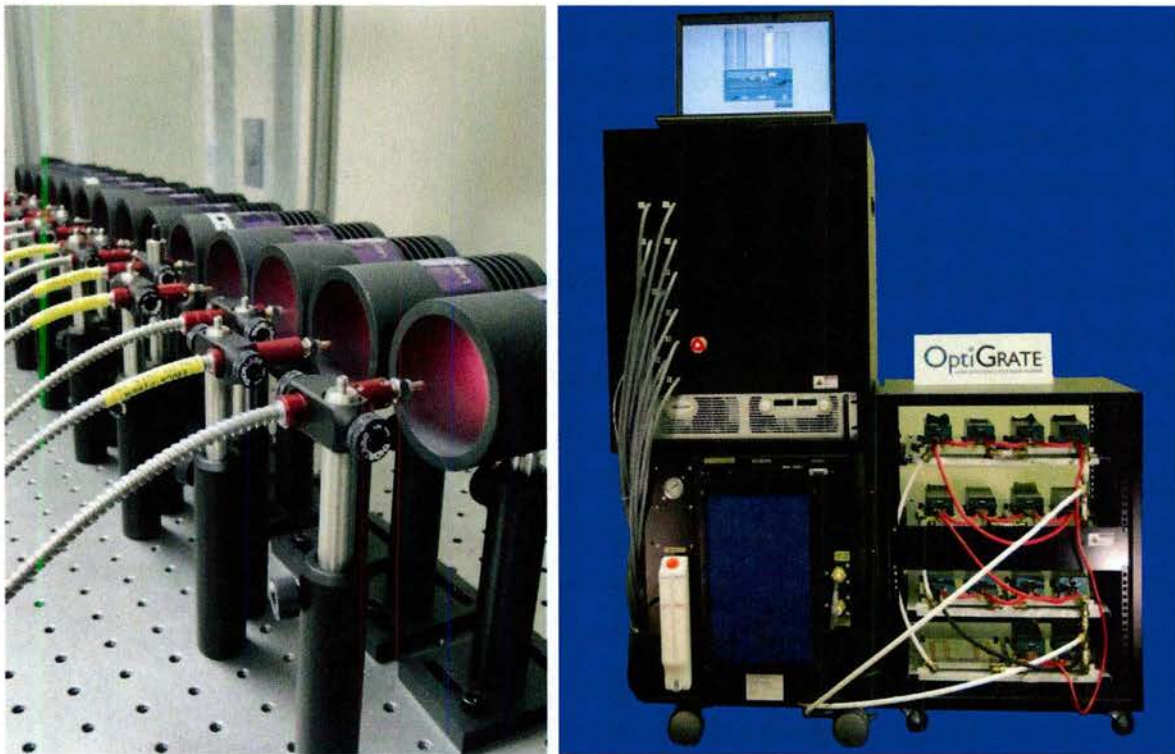


Fig. 27. Conversion of scientific results to practical devices – OptiGrate Corporation delivered to AFRL 750 W in 25 pm at 780 nm.

Thus, volume Bragg gratings in a photo-thermo-refractive glass with extremely narrow spectral selectivity (17-20 pm / 8.4-9.9 GHz @ 780 nm) and perfect uniformity were recorded. Low absorption coefficient at a laser wavelength and correspondent low heating makes it possible to use these gratings to lock high power LD bars in external resonator architecture. The 230 W output power multi-channel diode laser with spectral line-width of 10 GHz (at 780 nm) and spectral contrast of 23 dB was demonstrated. Total power penalty of a spectrally narrowed and stabilized laser system was below 10%. This laser provides total absorption of radiation in low pressure alkali vapor gain media for DPAL. The described above modular architecture provides a narrow band source scalable to extremely high power levels. Such systems can be used not only for efficient Rb DPALs gain-medium cells but also for analogous K (potassium) and Cs (cesium) ones along with other optically pumped rarefied gas devices.

The work on integration of high power pumping modules was continued at OptiGrate Corp. Additional fiber coupled 14 modules were fabricated and integrated with the previous delivered modules in a single pumping system with 21 delivery fibers (Fig. 27). Total optical output power is 750 W, central wavelength is 780.027 nm (in air), spectral width (FWHM) - 22.5 pm, wavelength tuning range - 150 pm, spectral drift (Long-Term) less than 5 pm. Radiation is delivered to experimental Rb laser by means of 21 600 μ m diameter fibers with NA = 0.22. To the best of our knowledge this is the pumping laser system with record spectral brightness.

1.6. Extreme wide aperture single diodes for pumping Cs and Rb vapors

While a kilowatt class pumping system is developed and actively used at AFRL for experiments with low pressure Rb vapor, new goals appeared which are simplification of narrow band diode laser systems and dramatic decrease of size and cost of pumping systems. One of the possible approaches is the use of newly developed single diodes with waveguide width approaching 1 mm and power in CW regime ranged from 20 to 30 W (Fig. 28). This approach enables eliminating part of complex optical elements, such as beam transforming system, simplifies alignment and enables new, more compact design of pumping system.

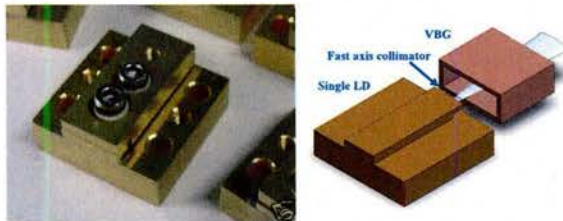


Fig. 28. The use of high power single diodes for pumping alkali vapors.

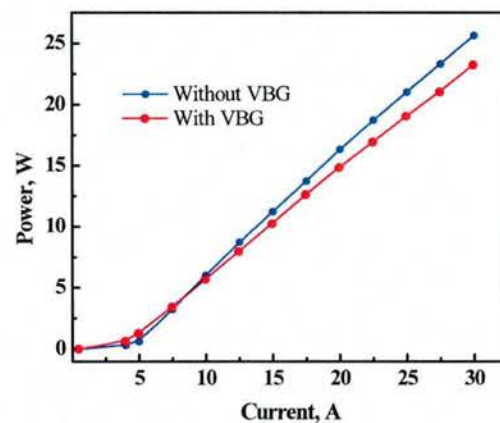


Fig. 29. Emitting power versus pumping current for 1-mm-wide laser diode emitting at 852 nm.

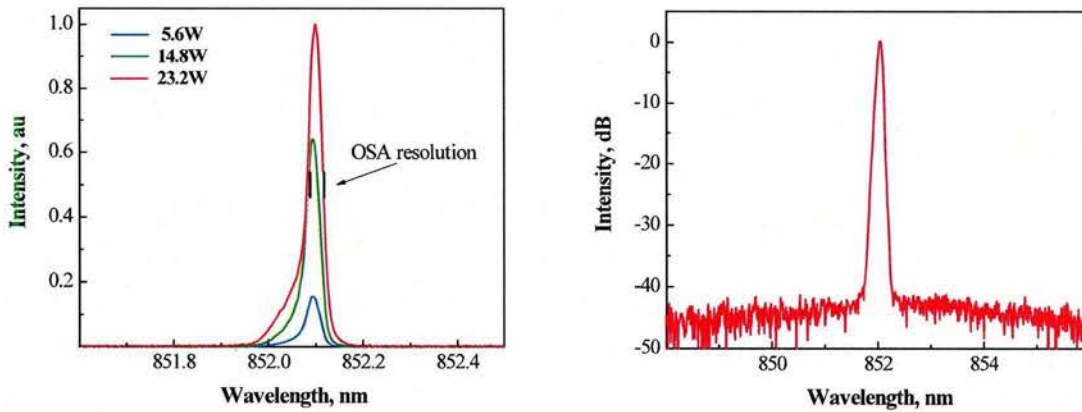


Fig. 30. Emission spectra of a single laser diode at different output power. Left – linear scale, right – logarithmic scale.

The first experiments were conducted with a commercially available LD with a stripe width of 1 mm that emits up to 25 W at 852 nm. Fast axis of the emitted beam was collimated and had a diffraction limited divergence. Slow axis divergence is about 10° similar to conventional diodes. It was not necessary to collimate slow axis to lock the diode to a narrow line. It was found that locking by an external VBG provides small decrease of threshold and about 8% decrease of output power (Fig. 29).

Emission spectra of this high power single diode are shown in Fig. 30. One can see that even for such a wide stripe and no collimation along the slow axis, spectral width of stabilized diode is within 25 pm. It was found that this spectral locking is stable up to a full pumping current and the main fraction of emitted power is concentrated within the main spectral lobe. The spectral contrast for a single LD exceeds 40 dB that is about 10 dB higher than that for a LD bar.

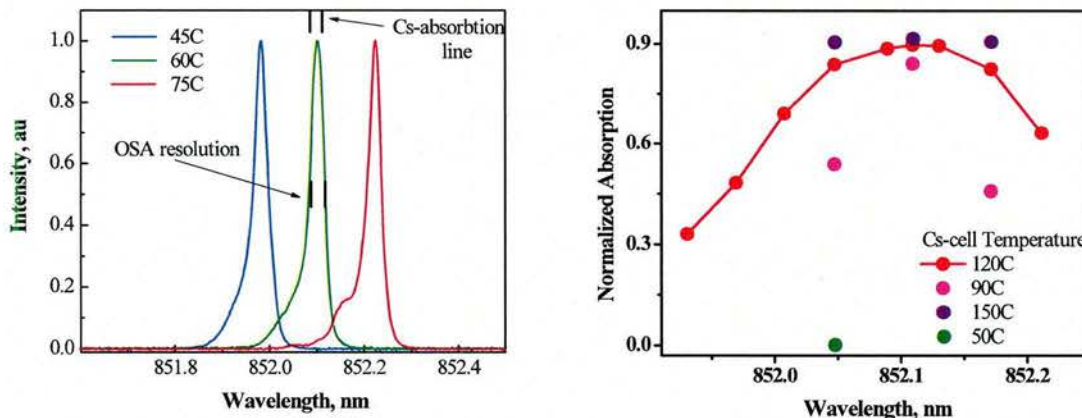


Fig. 31. Thermal tuning of emission spectrum of 1-mm-wide single laser diode.

Fig. 32. Dependence of absorption of laser radiation by a Cs cell on central wavelength for different temperatures of the cell.

Spectral tuning of the single laser diode was produced, as described above, by temperature control of a VBG that provided feedback. It is clear that this tuning for a single diode is more stable than that for a laser diode bar because no smile exists and no deflection of controlled radiation is observed. Tunability of this diode is shown in Fig. 31.

Dependence of absorption of radiation of the narrowed laser diode on wavelength is shown in Fig. 32. One can see that absorption of Cs dramatically depends on temperature of the cell. It was found that at the recommended temperature of 120°C more than 90% of radiation is absorbed by the cell. This laser system was delivered to US AF Academy and it is actively used for experiments with Cs lasers.

Similar experiments were conducted a commercially available LD with a stripe width of 1 mm that emits up to 20 W at 780 nm. Fast axis of the emitted beam was collimated and had divergence close to the diffraction limit. Slow axis divergence is about 10° similar to that for conventional diodes. It was not collimated. Locking by an external VBG provides small decrease of threshold and about 4% decrease of output power (Fig. 33). It is important to note that we had no chance to optimize reflection at the front end of the laser diode used for experiments. This means that for development of a high power pumping system this parameter could be optimized and power losses could be negligible low.

Emission spectra of a 1-mm-wide single diode are shown in Fig. 34. One can see that this LD is locked to a 15 pm wide emission line. This spectral locking is stable up to a full pumping current. The measured spectral contrast for a single LD is 30 dB. It was found that it is determined by noise in the detection system.

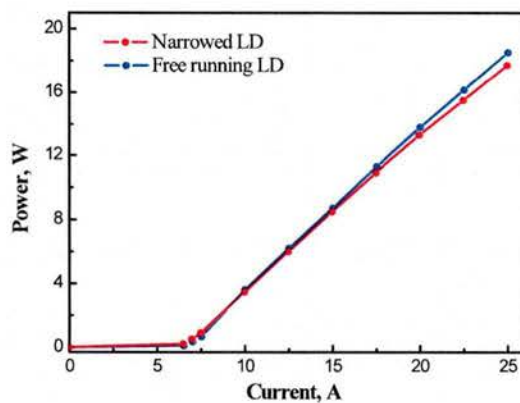


Fig. 33. Emitting power versus pumping current for 1-mm-wide laser diode emitting at 780 nm.

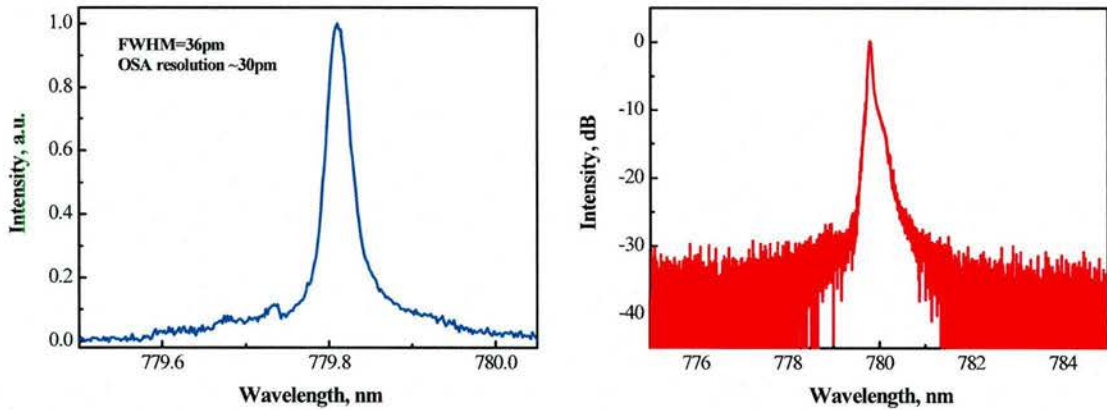


Fig. 34. Emission spectra of a single laser diode at different output power. Left – linear scale, right – logarithmic scale.

Thus, it is shown that newly developed and commercially available single laser diodes that emit up to 30 W CW radiation in spectral range 800-1000 nm could be reliably locked to narrow spectral lines below 30 pm that are necessary for pumping of low pressure Rb and Cs vapor lasers. This approach enables designing compact and robust pumping modules with high specific power density and very high spectral contrast.

1.7. Single diode for pumping metastable Ar laser

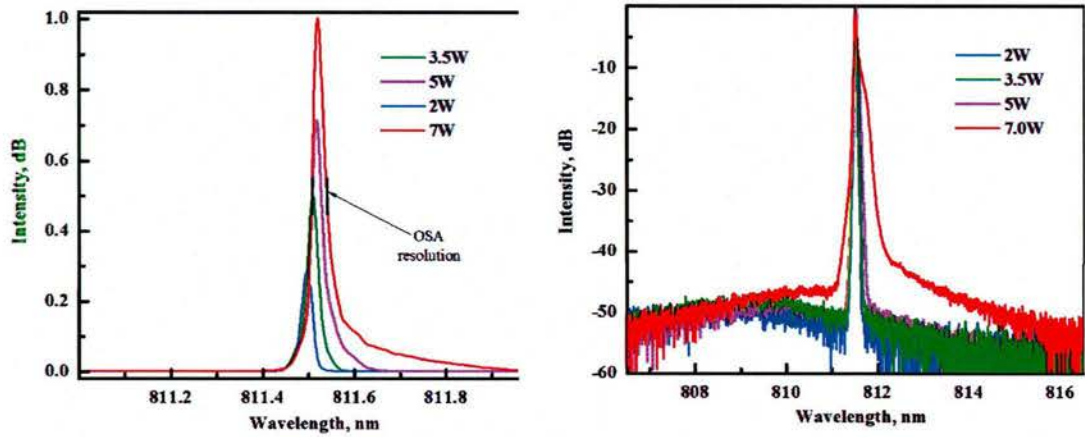


Fig. 35. Emission spectra of a single laser diode for Ar* pumping at different output power. Left – linear scale, right – logarithmic scale.

A new type of lasers was recently discovered by Dr. Heaven's group at Emory University which is based on optical pumping noble gases preliminary excited to the metastable levels. These

lasers are very promising because they do not require organic buffers and do not react with components of laser cells. Absorption spectra of those gases are narrow lines with spectral widths in the range of 20 pm. They are placed at 811.5, 811.7 and 882.2 nm for Ar*, Kr* and Xe*, respectively.

To provide an initial for experiments in CW regime we have developed and single laser diode pumping source emitting in the range of 811 nm. The same approach was used for a design of this laser. The fast axis of the emitted beam was collimated with divergence close to the diffraction limit. The slow axis was not collimated having about 8° divergence. Emission spectra of this laser are shown in Fig. 35. One can see that a single LD is locked to a narrow emission line with width below 20 pm. It was found that this spectral locking is stable up to a full pumping current. The spectral contrast for a single LD exceeds 40 dB that is about 10 dB higher than that for a LD bar. Thermal control of a VBG enabled fine tuning of an emission wavelength for 400 pm. The same laser can be used for both Ar* and Kr* pumping.

Figure 36 shows dependence of output power on pumping current. One can see that a commercially available LD with a stripe width of 100 mm emits up to 7 W. Locking by an external VBG provides small decrease of threshold and about 5% decrease of output power. This device was delivered to Emory university and was actively used for experiments with metastable Ar* and Kr* gas mixtures. The developed design would be used for development and fabrication of high power pumps for excitation of noble gases from metastable levels.

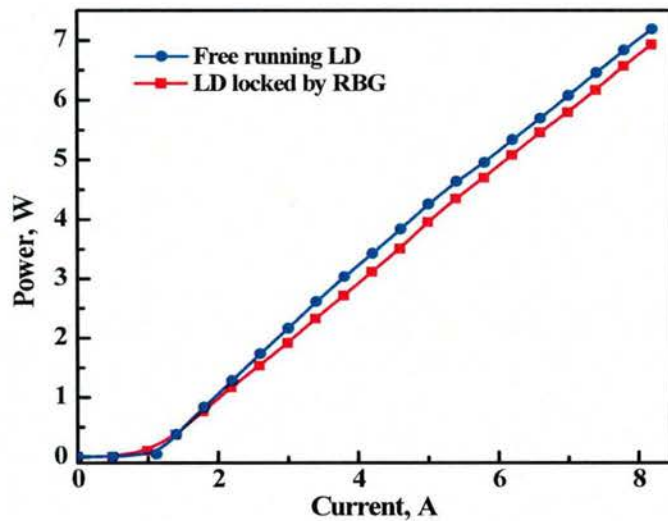


Fig. 36. Emitting power versus pumping current for 1-mm-wide laser diode emitting at 811 nm.

Section B. Work conducted at Emory University

1. Introduction

In recent years there have been concerted efforts to develop high power diode-pumped alkali vapor lasers (DPAL) for weapons applications.¹⁻¹³ These hybrid gas phase / solid state laser systems offer possibilities for constructing high-powered lasers with good beam quality. DPAL's utilize excitation of the alkali metal $^2\text{P}_{3/2} \leftarrow ^2\text{S}_{1/2}$ transition, followed by collisional relaxation and lasing on the $^2\text{P}_{1/2} \rightarrow ^2\text{S}_{1/2}$ line. Considerable progress has been made, including the demonstration of a 1 kW average power diode-pumped cesium laser¹⁴.

The outlook for scaling DPAL systems to 100 kW class devices in the near term remains promising. However, there are a number of engineering challenges. One set of problems is associated with heating the gas cell that contains the active medium in order to obtain sufficient metal vapor densities. For high-powered systems it is necessary to circulate the gas, which requires the construction of a heated flow system. This latter detail complicates the engineering, but is manageable. The harder problem stems from the chemically aggressive nature of the alkali metal vapors. In the presence of an intense light field, these reactants destroy the inner surfaces of the gain cell windows. A second set of problems is linked to the buffer gas that is used to induce spin-orbit relaxation between the ^2P levels. In a typical DPAL, He buffer gas is used to pressure broaden the absorption lines to improve the spectral overlap with the pump laser radiation. Unfortunately, He and the other rare-gases have low cross sections for spin-orbit relaxation. As the use of very high gas pressures degrades the beam quality of the laser, the solution has been to add a second buffer gas component that induces rapid spin-orbit relaxation, without significantly quenching the ^2P levels. Small hydrocarbons such as methane and ethane have proven to be effective. The downside of using these reagents is that they react with the alkali metals to produce hydrides ("laser snow") and carbonaceous deposits (particularly on the windows, where the reactions are facilitated by photoexcitation).

There is interest in developing DPAL analog systems in order to circumvent the chemical problems and expand the range of pump and lasing wavelength that can be employed. Unfortunately there are few alternate atomic systems when limiting the search to pumping atoms from the ground state. Within the scope of this program, the group at Emory University has explored the idea of using optical pumping of atoms that are in metastable electronic states.

2. Rare-gas spectroscopy and laser wavelengths

The rare-gases ($\text{Rg} = \text{He}, \text{Ne}, \text{Ar}, \text{Kr}, \text{and } \text{Xe}$) have fully occupied ground electronic configurations $ns^2 np^6$. Optical excitation of the ground state atoms requires wavelengths in the vacuum ultraviolet range. However, the lowest energy excited state of a rare-gas atom is metastable, and has an electronic configuration that resembles an alkali metal¹⁵. More specifically, the $np^5(n+1)s$ configuration yields four states, $^3\text{P}_{2,1,0}$ and $^1\text{P}_1$ (Fig. 1). Two of these states, $^3\text{P}_{2,0}$, are metastable with long radiative lifetimes¹⁶. For example, the $^3\text{P}_2$ and $^3\text{P}_0$ states of Kr have lifetimes of 67.7 and 0.45 s, respectively. These metastable states have strong $(n+1)s \rightarrow (n+1)p$ transitions in the far-red and near IR spectral regions¹⁷⁻²¹. Rg^* metastables can be

generated using a low-power electrical discharge. Concentrations of $(2-5) \times 10^{13}$ atoms/cm³ have been achieved and are ideal for laser development. Note that the power for the laser is supplied by optical pumping, and not by the discharge.

There are 10 electronic states that correlate with the $np^5(n+1)p$ configuration. Here we label these states using Racah notation of the form $n[K]_J$. The quantum numbers are defined as follows; n is the principal quantum number, l is the orbital angular momentum of the outer electron, $K=J_{core}+l$ and $J=K+S$. The J_{core} quantum number is associated with the electronic angular momentum of the $Rg^+ np^5$ core configuration which gives rise to a widely split, inverted 2P state. The lower energy component has $J_{core}=3/2$, which, when combined with the $(n+1)p$ outer electron of spin S , gives rise to six states (designated by $(n+1)p$). Combining $J_{core}=1/2$ with the $(n+1)p$ outer electron produces a further four states that are designated by $(n+1)p'$. Fig. 1 illustrates the energy level pattern of Kr^* where the states arising from the $4p^55s$ and $4p^55p$ configurations are shown. Both Racah notation and the older Paschen labels are presented in this diagram.

A laser scheme that mimics the alkali vapor system involves excitation of the $(n+1)s[3/2]_2 \rightarrow (n+1)p[5/2]_3$ transition and lasing on the $(n+1)p[1/2]_1 \rightarrow (n+1)s[3/2]_2$ line. The baseline scheme for building an optically pumped Kr^* laser is illustrated in Fig. 1. The system is pumped at 811.5 nm, has rapid collisional relaxation between the $5p[5/2]_3$ and $5p[1/2]_1$ states, and exhibits lasing back to the metastable $5s[3/2]_2$ state at 893.1 nm. The quantum efficiency is high, $\eta_{qe} = \lambda_p / \lambda_l = 0.91$, and the optical cross-section for absorption with 1000 Torr of Helium in the discharge is similar to the DPAL systems, $\sigma_{13} = 7.2 \times 10^{-13}$ cm². The state degeneracy's of, $g_3 = 7$, $g_2 = 3$ and $g_1 = 5$ are more favorable than the DPAL system, while the energy splitting of the Kr $5p[5/2]_3$ and $5p[1/2]_1$ states, $\Delta E_{32} = 1125.89$ cm⁻¹, is large enough to prevent significant back-transfer. The $s \rightarrow p$ transitions of the metastable rare-gas atoms are entirely analogous those of the alkali metals. They have similar transition probabilities, upper state radiative lifetimes, lasing wavelengths and ionization potentials. Relevant data for Ne, Ar, Kr and Xe are presented in Table 1¹⁷. The advantages of using Rg^* for the lasing medium are that heating is not required, rare-gas collision partners can be used for spin-orbit relaxation, and the entire system is chemically inert.

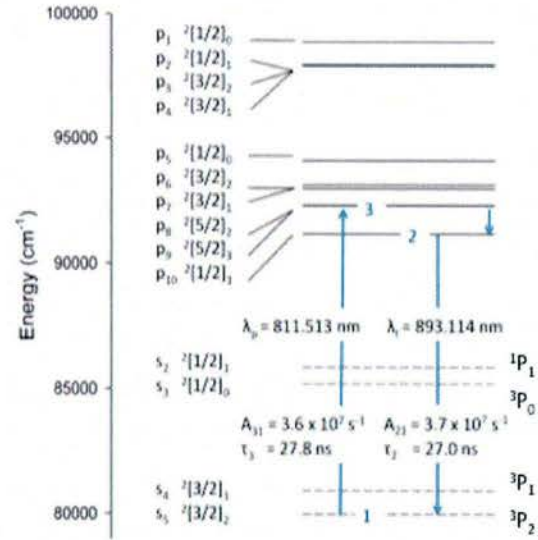


Figure 1. Rare gas laser transitions.

Table 1. Wavelengths, Einstein coefficients, and ionization energies for rare gas lasers.

Alkali	λ_p (nm)	λ_l (nm)	A_p (10^7 s $^{-1}$)	A_l (10^7 s $^{-1}$)	η_{qe}	I.P. ^a (eV)
Ne	640.402	703.435	5.14	2.53	0.91	4.97
Ar	811.658	912.547	3.31	1.89	0.89	4.23
Kr	811.513	893.114	1.30	3.70	0.91	4.10
Xe [*]	882.183	904.793			0.98	3.83

^aEnergy to ionize the atom from the $(n+1)s(3/2)_z$ state

Several schemes can be devised for the optically pump rare-gas lasers. In addition to the direct DPAL analog shown in Figure 1, lasing could be achieved using two alternative approaches: (1) lasing down to 3P_1 followed by relaxation to 3P_2 , and (2) excitation to higher p levels followed by collisional relaxation to adjacent or non-adjacent levels. A large number of possible pump and lasing wavelengths may be supported by most of the rare-gases. The wavelengths associated with s to p transitions for Kr are illustrated in Table 2. The wavelengths are longer for Xe (> 904 nm), offering better eye safety for HEL deployment.

3. Energy transfer kinetics

As a prelude to optical pumping studies, the group at Emory examined the pulsed discharge generation of Ne* and Kr* metastables, and collisional energy transfer processes for these atoms²². Figure 2 shows a schematic diagram of the experimental apparatus used to investigate the kinetics of $Rg(np^5(n+1)p) + Rg'$ collisions. A pulsed discharge was used to generate $Rg(np^5(n+1)s)$ metastables, which were then excited to specific $Rg(np^5(n+1)p)$ levels using a pulsed laser. A cylindrical (L=10 cm and W=4 cm) Pyrex discharge cell was used to contain the slowly flowing rare gas mixtures. Fused silica windows were attached to the ends of the cylindrical cell. A pair of stainless steel parallel-plate electrodes was mounted by tungsten rods inside the cell with a 2.0 cm inter-electrode spacing. A negative pulsed dc voltage of 800V was applied across the electrodes to generate the discharge plasma. The discharge period was 350 μ s, the repetition rate 10 Hz, and the maximum peak current ranged from 150 to 350 mA.

Table 2. Diversity of Kr wavelengths.

	Wavelengths, λ (nm) Kr $4s^24p^55s - 4s^24p^55p$			
	s_5	s_4	s_3	s_2
p_{10}	893.1	975.4	1673.2	1879.1
p_9	811.5	878.9	1407.9	1550.9
p_8	810.7	877.9	1405.4	1547.8
p_7	769.7	830.0	1286.6	1405.0
p_6	760.4	819.2	1260.8	1374.3
p_5	708.2	759.0	1123.5	1212.7
p_4	567.4	599.6	806.2	851.1
p_3	557.2	588.2	785.7	828.3
p_2	556.4	587.3	784.1	826.6
p_1	529.6	557.5	731.9	768.7

A rotary pump was used to evacuate the cell to a base pressure of 1.0 mTorr. Ultra-high purity grade (99.999%) neon, krypton and helium was used. These gases were further purified by passage through molecular sieve traps that were immersed in liquid nitrogen. The total gas pressure in the discharge cell was measured by a capacitance manometer (MKS Baratron).

Tunable radiation with spectral bandwidth of 0.3 cm^{-1} was produced from a dye laser pumped by the 308 nm output of an excimer laser running at 10 Hz (Lambda Physik EMG201/FL3002). The linewidth was determined from laser excitation spectra for the metastable Ne. A range of dye solutions (Rhodamine 610, Rhodamine 640, Oxazine 720, LDS 798 and LDS 867 laser dyes) were used to excite the $3p[3/2]_2$, $3p[3/2]_1$, $3p[5/2]_2$, $3p[5/2]_1$ level of Kr($4p^5 5p$).

The output from the dye laser was directed between the electrodes in the discharge cell. Fluorescence was collected along an axis that was perpendicular to the laser light propagation. A biconvex lens was used to focus the fluorescence onto the entrance slit of a 0.64 meter monochromator (Instruments SA HR-640, 1200 g/mm grating). At the exit slit, the dispersed fluorescence was detected by a photomultiplier tube (PMT) (RTL, B2/RFI). The output from the PMT was processed by a boxcar integrator (Stanford Research Systems, SR 250) for the recording of emission spectra. Time resolved signals were recorded with the monochromator set to transmit the light from a single emission line. The temporal profiles were captured by a 150 MHz oscilloscope (Tektronix TDS 1012). Typically, 128 laser shots were averaged to obtain results with good signal to noise ratios. For the analysis of the peak intensity data of the emission spectra, knowledge of the wavelength dependence of the relative detection efficiency was needed. Variation of the response of the monochromator/PMT combination in the 600-900 nm region was calibrated using a tungsten lamp.

All measurements for Ne were made with the laser set to excite the metastables 450 ms after the cessation of the discharge. The delay of the dye-laser pulse relative to the termination of the electrical discharge was controlled by a digital delay generator (Stanford Research Systems DG535). Time-resolved fluorescence signals for Ne ($2p^53p$) at varying pressures of the He buffer gas were recorded to obtain total depopulation rate constants for a chosen initial level. Time integrated fluorescence spectra were measured by fixing the dye laser wavelength on a specific $2p^53p-2p^53s$ transition and scanning the monochromator through the region that covered the emission lines of the initially populated state, and those of the levels populated by collisional

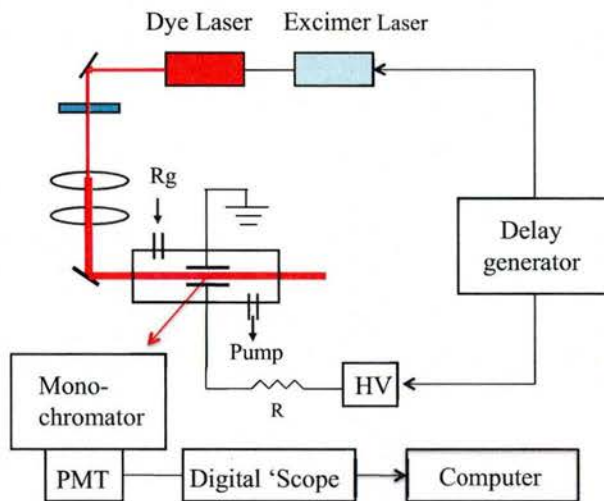


Figure 2. Schematic diagram of the apparatus used to observe Rg* fluorescence decay kinetics.

energy transfer. A boxcar gate width of 100 ns was used for these measurements. These spectra were corrected for the wavelength dependent response of the detection system.

Measurements of Kr($4p^55p$)+Rg transfer rate constants for Rg=He, and Kr were carried out using the techniques described above. The deactivation of Kr ($4p^55p$) $5p[1/2]_1$ was examined using excitation of the $5p[1/2]_1 \leftarrow 5s[3/2]_2$ transition (892.9 nm) followed by detection of the $5p[1/2]_1 \rightarrow 5s[3/2]_1$ line (975.2 nm). Relatively rapid decay of the Kr ($4p^55s$) metastables was observed at the termination of the discharge pulse. Owing to this circumstance, the LIF measurements were made during the discharge pulse.

Total Helium deactivation rate constants for the Ne $2p^53p$, $J_{core}=3/2$ states.

Rate constants were measured for the total depopulation of the five lowest energy Ne($2p^53p$), $J_{core}=3/2$ states. All of these states are optically connected to the states of the Ne ($2p^53s$) configuration by electric dipole allowed transitions. Laser excitation occurred 450 μ s after the discharge, by which time the fluorescence from the discharge excited plasma had decayed to an insignificant level. However, the Ne ($2p^53s$) levels are long-lived, and a substantial concentration of metastable Ne was present at the chosen delay. From optical absorption measurements, made with the dye laser tuned to the center of the $3p[3/2]_2-3s[3/2]_2$ line, the density of the metastable states in our experiment was estimated to be on the order of 10^{11} cm^{-3} .

The total depopulation rate constant for transfer out of a selected Ne($2p^53p$) level was measured by time-resolving the fluorescence from the initially excited level. Where possible, the emission line monitored was not the same as the excitation line, in order to avoid interference from scattered laser light. As an example, Fig. 3 shows the fluorescence signal obtained by excitation of the $3p[3/2]_2 \leftarrow 3s[3/2]_2$ transition with detection of the $3p[3/2]_2 \rightarrow 3s[1/2]_1$ emission. Note that the curve shows a finite rise time and rounded maximum (Fig. 3a) because the duration of the excitation pulse is comparable to the fluorescence decay lifetime. As described below, the temporal profile of the laser pulse can be modeled as a Gaussian

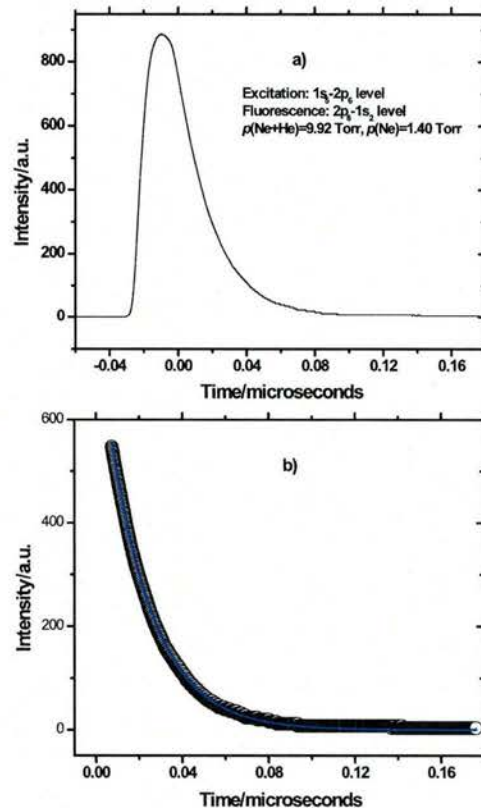


Figure 3. Fluorescence decay curves for the $3p[3/2]_2$ level of Ne($2p^53p$) in the presence of Ne (1.4 Torr) and He (8.5 Torr). The line in trace b is a fitted single exponential decay function.

function with a full width at half maximum (FWHM) of 12 ns. Consequently, the segment of the decay curve starting 10 ns after the maximum of the laser pulse was used to characterize the fluorescence decay rate. Fig. 3b show a plot of this segment of the data, along with the line generated by fitting a single exponential decay function to the data. This example gave a good fit to a single exponential decay, as did the corresponding curves for population transfer out of the other $\text{Ne}(2p^53p)$ levels examined in this study.

The observation of single exponential decay kinetics indicates that back transfer into the initially populated level is unimportant. Hence the decay of population from an initially populated state i can be represented by the expression

$$[i] = [i]_0 \exp(-R_{T,i}t) \quad (1)$$

where $[i]$ indicates the concentration of state i , $[i]_0$ is the initial concentration at time $t=0$ (defined by the effective end of the laser pulse) and $R_{T,i}$ is the total removal rate. The latter is defined by

$$R_{T,i} = \Gamma_{rad} + (k_{q,i}^{He} + \sum_f k_{f,i}^{He})[\text{He}] + (k_{q,i}^{Ne} + \sum_f k_{f,i}^{Ne})[\text{Ne}] \quad (2)$$

where Γ_{rad} is the radiative decay rate and $k_{f,i}^M$ is the rate constant for transfer from state i to final state f induced by collision with the species M (He or Ne). The rate constants for transfer to

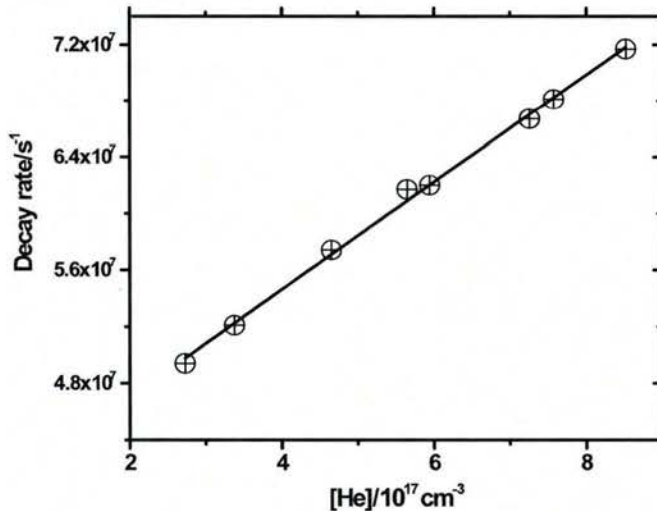


Figure 4. Dependence of the $\text{Ne}(2p^53p)3p[3/2]_2$ fluorescence decay rate on [He] with [Ne] held constant at $4.5 \times 10^{16} \text{ cm}^{-3}$.

levels that are not members of the $2p^53p$ multiplet are designated by k_{qj}^M . In the following, the rate constant for total removal of population from state i by collisions with He is given as

$$k_{T,i}^{He} = k_{q,i}^{He} + \sum_f k_{f,i}^{He} \quad (3)$$

To determine the $k_{T,i}^{He}$ values, total decay rates were measured for He pressures in the range of 10-30 Torr, with the Ne pressure held constant (at 1.4 Torr for most cases). For these data, plots of $R_{T,i}$ vs. [He] (often referred to as a Stern-Volmer plot), such as the example shown in Fig. 4,

have a slope of $k_{T,i}^{He}$ and intercept of $\Gamma_{rad} + k_{T,i}^{Ne}[\text{Ne}]$. The He total removal rate constants determined from this model are listed in Table 3. For comparison, Table 3 also includes the Ne total removal rate constants determined by Chang and Setser²³.

Table 3. Total removal rate constants for $\text{Ne}(2p^53p)$ with He and Ne

Level	$\text{Ne}(2p^53p)+\text{He}$, Present work	$\text{Ne}(2p^53p)+\text{Ne}$, Ref. 12
	$k_T^{He} (10^{-11} \text{ cm}^3 \text{s}^{-1})$	$k_T^{Ne} (10^{-11} \text{ cm}^3 \text{s}^{-1})$
$3p[3/2]_2$	3.8 ± 0.5	1.2 ± 0.4
$3p[3/2]_1$	4.7 ± 1.0	0.9 ± 0.2
$3p[5/2]_2$	4.5 ± 1.0	1.8 ± 1.4
$3p[5/2]_3$	6.3 ± 1.2	4.4 ± 1.1
$3p[1/2]_1$	1.7 ± 0.3	1.7 ± 0.5

He + Ne(2p⁵3p) state-to-state transfer rate constants.

A combination of time- and wavelength-resolved fluorescence measurements were used to characterize the collisional transfer processes following single-level level excitation of $\text{Ne}(2p^53p)$. Analysis of the state-to-state transfer data was conducted in two stages. First, an approximate analytical model was applied to extract a preliminary set of rate constants. These were then used as the starting values for full master equation simulations of the time- and wavelength-resolved fluorescence data. The final rate constant set was obtained by systematic adjustment of the rate constants in the numerical simulations.

To obtain analytical expressions for the time-dependent state populations, we start by considering a model where all back-transfer processes are neglected. The initially populated level can only lose population, and the collisionally populated levels only receive population from the initially excited state. This is a good approximation when the number of transfer collisions experienced during radiative decay is small. For this assumption the time dependence of $[i]$ is given by Eq. 1 above. The rate equation for a collisionally populated level is given by

$$\frac{d[i]}{dt} = R_{f,i}[i] - R_{T,f}[f] \quad (4)$$

with $R_{f,i} = k_{f,i}^{He}[\text{He}] + k_{f,i}^{Ne}[\text{Ne}]$. Substitution of Eq. 1 in Eq. 4 and integration yields the expression

$$[f] = \frac{R_{f,i}[i]_0}{(R_{T,i} - R_{T,f})} (\exp(-R_{T,f}t) - \exp(-R_{T,i}t)) \quad (5)$$

The time-integrated fluorescence spectra have line intensities that are proportional to the time-integrated level populations. As the boxcar gate width was sufficient to collect >90% of the emitted light, we can approximate the time-integrated populations by

$$P_i = \int_0^\infty [i] dt = \frac{[i]_0}{R_{T,i}} \quad \text{and} \quad P_f = \int_0^\infty [f] dt = \frac{R_{f,i}[i]_0}{R_{T,i}R_{T,f}} \quad (6)$$

The ratios of these terms are then related to the ratios of the time-integrated fluorescence intensities by the expression

$$\frac{P_f}{P_i} = \frac{R_{f,i}}{R_{T,f}} = \frac{(I_{f,l}/A_{f,l})}{(I_{i,l}/A_{i,l})} \quad (7)$$

where $I_{f,l}$ is the observed intensity of the transition from state f to the lower level l (after correcting for the instrumental response function) and $A_{f,l}$ is the radiative decay rate for the $f \rightarrow l$ transition. The values determined by Chang and Setser¹¹ were used for the radiative decay rates. The rates in Eq. 7 include contributions from collisions with both He and Ne. However, as the spectra were recorded under conditions with $[\text{He}] \gg [\text{Ne}]$, the contributions from $\text{Ne}(2p^53p) + \text{Ne}$ collisions were neglected at this stage of the analysis. With this additional approximation the state-to-state rate constants can be estimated from the expression

$$k_{f,i}^{He} \approx \frac{(I_{f,l}/A_{f,l})}{(I_{i,l}/A_{i,l})} k_{T,i}^{He} \quad (8)$$

Preliminary state-to-state rate constants were derived using Eq. 8. Estimates for the $k_{q,i}^{He}$ rate constants were obtained by application of Eq. 3.

Master equation modeling was used to refine the rate constants. The coupled differential rate equations for this problem are given by

$$\frac{d[i]}{dt} = S(t) + \sum_n R_{i,n}[n] - R_{T,i}[i] \quad (9)$$

and

$$\frac{d[f]}{dt} = \sum_n R_{f,n}[n] - R_{T,f}[f] \quad (10)$$

where $S(t)$ defines the excitation of the initial state by the laser pulse. This was represented by a Gaussian function with a FWHM of 12 ns. The contributions from $\text{Ne}(2p^53p) + \text{Ne}$ collisions were included using the rate constants of Chang and Setser²³.

Equations 9 and 10 were solved by standard numerical integration techniques. The results were used to simulate both the time- and wavelength-resolved fluorescence data. As exothermic transfer was generally more efficient than endothermic transfer, the strategy for refining the rate constants was to start with data for initial excitation of the lowest energy level ($3p[1/2]_1$) and progress to initial states with successively higher energies. Transfer from $3p[1/2]_1$ to other states in the $2p^53p$ manifold was inefficient, such that almost all of the population loss could be attributed to transfer to other multiplet states (i.e., $k_{q,x}^{He} \approx k_{T,x}^{He}$, $x=3p[1/2]_1$). Going to higher energies, the numbers of levels significantly involved in the energy transfer processes increased. However, the number of rate constants to be modified at each step was kept to a minimum as the sub-set of rate constants for the lower levels had already been subject to an iteration of refinement. The state-to-state rate constants were constrained using the principle of detailed balance and refined by performing multiple optimization cycles.

As examples of the quality of the final fits obtained from the master equation model, comparisons of the measured and simulated data for $i=3p[3/2]_2$ for the time-resolved fluorescence data are presented as the broken curves in Figs 5. Note that the intensities in Fig. 5 are arbitrary, and it is the fit to the time dependence that was optimized. The optimized rate constants for $\text{Ne}(2p^53p) + \text{He}$ energy transfer are collected in Table 4.

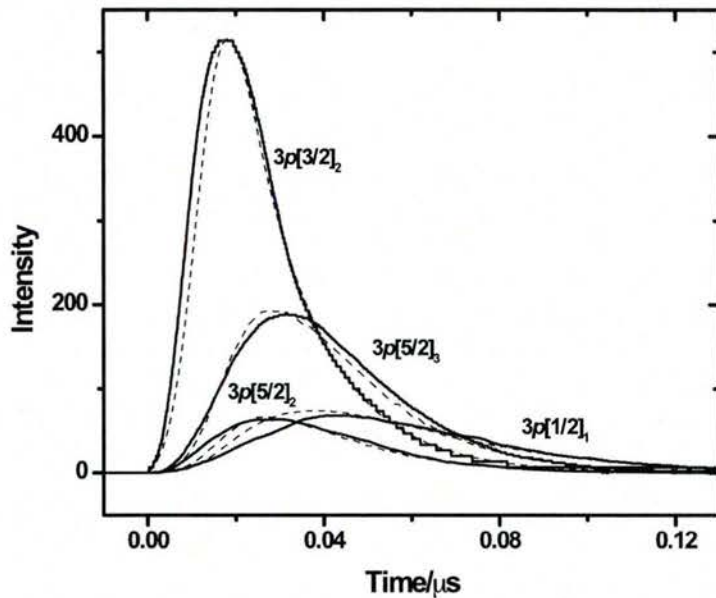


Figure 5. Time resolved fluorescence signals following excitation of $\text{Ne}(2p^53p) 3p[3/2]_2$ in the presence of 1.4 Torr of Ne and 26.6 Torr of He.

Table 4. Energy transfer rate constants for $\text{Ne}(2p^53p) + \text{He}$

$i \setminus f$	$3p[3/2]_2$	$3p[3/2]_1$	$3p[3/2]_2$	$3p[3/2]_1$	$3p[5/2]_2$	$3p[5/2]_3$	$3p[1/2]_1$	Σk_{if}
$3p[3/2]_2$	0.0	0.03	0.0	1.3	0.8	0.9	0.7	3.7
$3p[3/2]_1$	0.01	0.02	0.9	0.00	1.1	1.7	1.4	5.1
$3p[5/2]_2$	0.0	0.0	0.08	0.2	0.0	2.8	2.3	5.4
$3p[5/2]_3$	0.0	0.0	0.03	0.08	0.8	0.0	1.9	2.8
$3p[1/2]_1$	0.0	0.0	0.0	0.0	0.002	0.005	0.00	0.007

Units are $10^{-11} \text{ cm}^3 \text{ s}^{-1}$. Errors are estimated to be 25%.

$Kr(4p^55p)$ + Rg total removal rate constants.

The total depopulation rate constants for transfer out of a selected $Kr(4p^55p)$ level was measured by time-resolving the fluorescence from the initially excited levels. Where possible, the emission line monitored was not the same as the excitation line, in order to avoid interference from scattered laser light. Single exponential decay curves were observed, and the total removal rate constants were derived from Stern-Volmer plots such as those shown in Fig. 6. The rate constants measured to date are collected in Table 5.

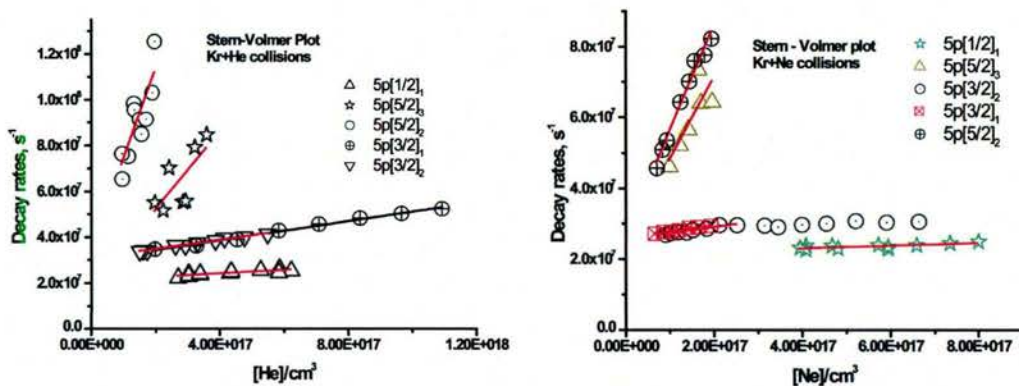


Figure 6. Stern-Volmer plots of the decay rates for $Kr(4p^55p)$ states as functions of He and Ne number density

Table 5. Total depopulation rate constants for $Kr(4p^55p)$ colliding with He, Ne, and Kr at T=300 K.

Kr Levels	Expt. k^{Kr-Kr}_{Tot} ($10^{-11} \text{ cm}^3 \text{s}^{-1}$)	Expt. k^{Kr-He}_{Tot} ($10^{-11} \text{ cm}^3 \text{s}^{-1}$)	Expt. k^{Kr-Ne}_{Tot} ($10^{-11} \text{ cm}^3 \text{s}^{-1}$)	Chang et al. ¹⁸ k^{Kr-Ar}_{Tot} ($10^{-11} \text{ cm}^3 \text{s}^{-1}$)
$5p[3/2]_2$	2.1 ± 0.5	1.9 ± 0.5	1.7 ± 0.2	2.5 ± 0.8
$5p[3/2]_1$	3.5 ± 1.0	3.2 ± 0.5	1.8 ± 0.5	0.65 ± 0.30
$5p[5/2]_2$	34.8 ± 3.5	36.6 ± 4.0	29.9 ± 5.0	26.8 ± 4.0
$5p[5/2]_3$	20.9 ± 7.0	16.9 ± 8.0	20.8 ± 8.0	17.8 ± 2.5
$5p[1/2]_1$	7.2 ± 0.5	$<0.6 \pm 0.2$	$<0.4 \pm 0.2$	12.2 ± 0.6

State-to-State Energy Transfer Rate Constants for $Kr(4p^55p)$ + Rg

Collisional energy transfer pathways were initially examined by recording dispersed fluorescence spectra following single-level excitation. For these measurements, the fluorescence was time-integrated using a boxcar integrator. As an example, Fig. 7 shows a spectrum obtained using excitation of the $Kr\ 5p[3/2]_2 \leftarrow 5s[3/2]_2$ transition in the presence of He at a pressure of 22.5 Torr. Here it can be seen that the $5p[3/2]_1$ and $5p[5/2]_3$ levels are being populated by collisional energy transfer. Dispersed fluorescence spectra were recorded for excitation of the $5p[3/2]_2$, $5p[3/2]_1$, $5p[5/2]_2$, $5p[5/2]_3$, and $5p[1/2]_1$ levels, in the presence of He, Ne and Kr buffer

gas. For excitation of the $5p[1/2]_1$ level, which is the lowest energy state of the multiplet, a small fraction of upward energy transfer to the $5p[5/3]_2$ level was the only process evident in the spectra. The other potentially active channel of quenching to the lower excited state $4p^55s$ manifold could not be observed in the wavelength range examined.

Time-resolved fluorescence signals were recorded by monitoring the intensities of specific spectral lines (fixed wavelength detection). State-to-state energy transfer rate constants were derived using the two-step analysis method described above. The rate constants obtained from studies of Kr*+Kr and Kr*+He are collected in Tables 6 and 7.

Table 6. State-to-state rate constants for Kr($4p^55p$) colliding with Kr.

$i \setminus f$	5p[1/2] ₀	5p[3/2] ₂	5p[3/2] ₁	5p[5/2] ₂	5p[5/2] ₃	5p[1/2] ₁
5p[3/2] ₂	0.2	0.0	0.7 (0.07)	0.58 (0.5)	0.5 (2.2)	0.1 (0.02)
5p[3/2] ₁	0.0	0.6	0.0	1.4	0.9	0.6
5p[5/2] ₂	0.0	3.6	2.2 (1.8)	0.0	24.5 (26.2)	4.5 (8.1)
5p[5/2] ₃	0.0	0.3	0.1	17.7 (16.8)	0.0	2.7
5p[1/2] ₁	0.0	0.002	0.03	0.02	0.02	0.00

The rate coefficients are given in units of $10^{-11} \text{ cm}^3 \text{s}^{-1}$. Errors are estimated to be $\pm 25\%$.

Table 7. State-to-state rate constants for Kr($4p^55p$) colliding with He.

$i \setminus f$	5p[3/2] ₂	5p[3/2] ₁	5p[5/2] ₂	5p[5/2] ₃	5p[1/2] ₁
5p[3/2] ₂	0.0	1.2	0.4	0.3	0.1
5p[3/2] ₁	1.1	0.0	1.1	0.8	0.2
5p[5/2] ₂	0.6	0.1	0.0	33.1	2.3
5p[5/2] ₃	0.2	0.2	15.9	0.0	0.7
5p[1/2] ₁	0.0	0.0	0.006	0.0	0.0

The rate coefficients are given in units of $10^{-11} \text{ cm}^3 \text{s}^{-1}$. Errors are estimated to be $\pm 25\%$.

4. Gain and lasing of optically pumped metastable rare gas atoms using pulsed excitation

Experimental method

In order to achieve rapid collisional energy transfer in the gain and lasing experiments, it was necessary to use a gas discharge that could operate at relatively high pressures. For these proof-of-principle studies we used the discharge cavity of a commercial excimer laser (Lambda Physik EMG 102) to produce discharges in Rg/He mixtures and pure Ar. Observations of gain and lasing from optically pumped Rg* were carried out using the configuration shown in Fig. 8. The pulsed discharge was operated at its preset minimum voltage of 18 kV. The electrodes in this cavity are separated by approximately 2.5 cm, and have a length of 80 cm. The output coupler, M₁, was an uncoated MgF₂ window. For gain measurements, M₂ was also an uncoated window. To observe lasing M₂ was replaced by a total reflector and the probe laser was not used.

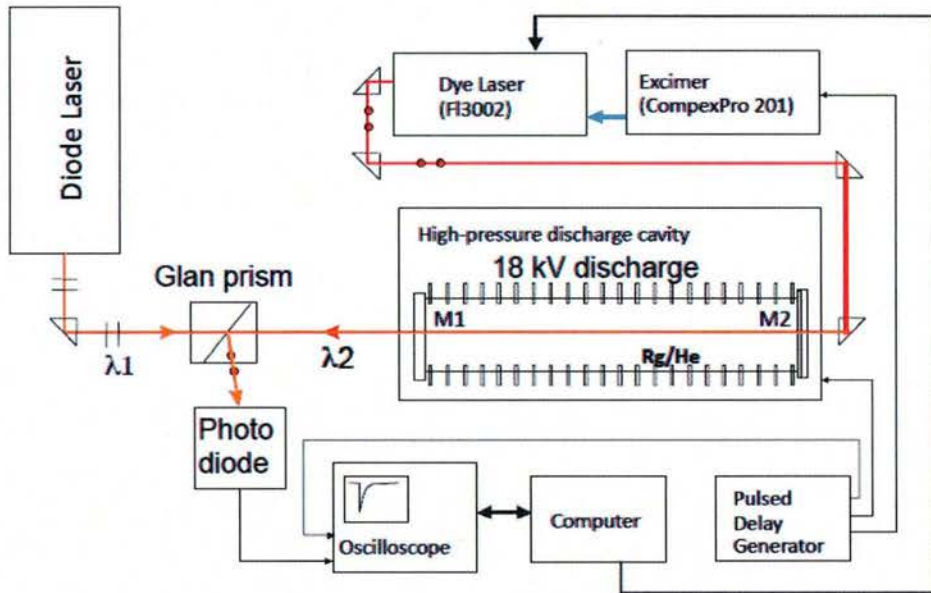


Figure 8. System used to study gain and lasing of optically pumped Rg*

Measurements were conducted with static fills of the gas mixtures in the discharge cavity. The cavity was first pumped down to 0.5 mbar and then flushed using pure He. To produce gas mixtures, a small quantity of the working gas (typically around 30 mbar of Ne, Ar, Kr, or Xe) was added to the chamber. The system was then filled with He to the desired total pressure (200-2000 mbar). In one series of experiments the discharge cavity was filled with pure Ar. Ultra-high purity gases were used as provided by the manufacturer, without further purification. The discharge was operated at a repetition frequency of 10 Hz. Following the discharge pulse (nominally 10 ns duration) the Rg* metastables were excited by the 10 ns pulses from a tunable optical parametric oscillator (OPO). For the wavelengths of interest, the OPO yielded pulse energies of around 0.25 mJ with a linewidth of 30 GHz. The pump beam diameter inside the discharge cavity was 0.4 cm. An electronic delay generator was used to control the delay between the discharge and OPO pulses. Some care was needed for this adjustment, as high

number densities resulted in strong absorption of the pump radiation. When the optical thickness was too great, only a limited segment of the optical path could be pumped to inversion.

A pulsed tunable dye laser (Lambda Physik CompexPro 201/FL3002) was used to test for optical gain. This instrument had a linewidth of 10 GHz and a pulse duration of approximately 10 ns. The dye laser output was attenuated to avoid saturation. As shown in Fig. 8, the horizontally polarized pump beam and the vertically polarized probe beam were counter-propagated through the discharge cavity. On exiting the cavity, the probe beam was directed to a photodiode by a Glan-Taylor polarizer.

The light exiting the cavity was directed by the polarizer to a monochromator/ photo-detector combination that was used to record the output spectrum. A 0.20 m monochromator (Bausch and Lomb) was used for these measurements. The output power was measured directly after the polarizer, using a commercial power meter (Ophir model 3A-P-V1-ROHS). The lasing spot was also imaged using an IR viewing card.

Results

The first experiments examined optical pumping of Kr* in Kr/He mixtures. To test the apparatus, the $5p[3/2]_1 \leftarrow 5s[3/2]_2$ transition was excited (769.67 nm, vacuum), and gain was measured on the $5p[3/2]_1 \rightarrow 5s[3/2]_1$ line (830.04 nm). As these transitions have a common upper level, measurements were made for the lowest possible total pressure (200 mbar, set by the interlock on the power supply) to minimize collisional relaxation. Fig. 9 shows results from this experiment. The lower trace is

a scan over the $5p[3/2]_1 - 5s[3/2]_1$ line, without optical pumping. A weak absorption at the line-center was observed. The scan with the pump laser on-resonance shows robust gain. Transmission intensities for the probe laser on- and off-resonance indicated a single-pass gain in excess of 100.

The objective of the second series of experiments was to see if gain could be observed using the DPAL analog pumping scheme illustrated in Fig. 10 (pumping at 811.51 with lasing at 893.12 nm). The initial investigation was carried out using 27 mbar of Kr in 973 mbar of He, and the results are shown in Fig. 10. Baseline signal levels were established, in the absence of the discharge, for the probe laser alone and the combination of the pump and probe lasers (left hand segment of the trace). The discharge was

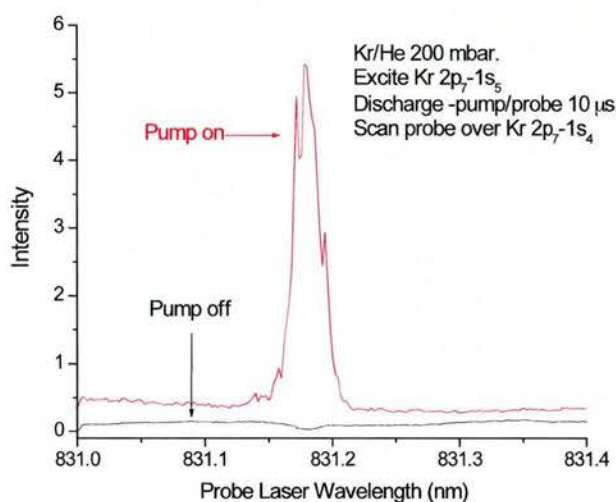


Figure 9. Demonstration of gain on the $5p[3/2]_1 - 5s[3/2]_1$ transition of Kr (27 mbar) in He. The upper and lower traces were taken with and without optical pumping of the $5p[3/2]_1 - 5s[3/2]_2$ transition.

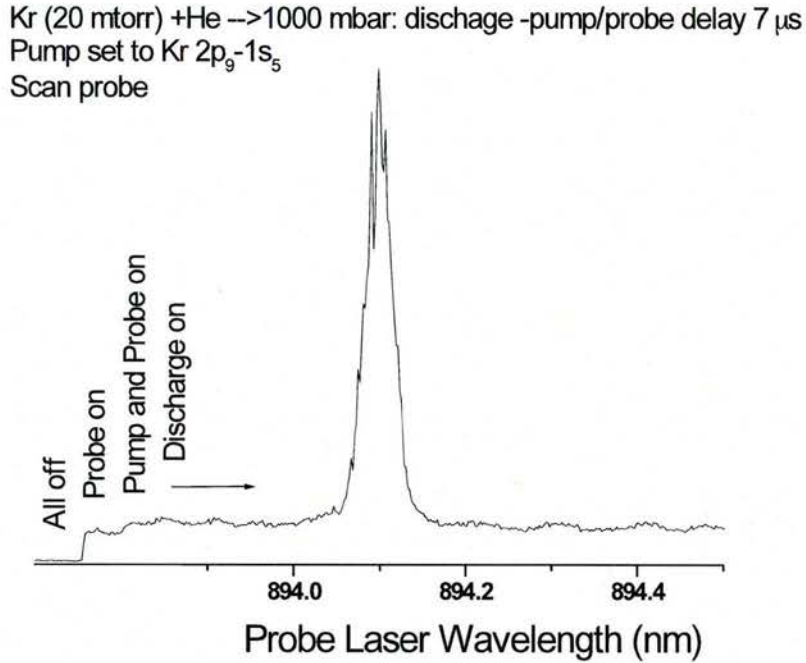


Figure 10. Demonstration of gain on the 5p[1/2]₁-5s[3/2]₂ transition of Kr (27 mbar) in He (973 mbar) following optical pumping of the 5p[3/2]₃-5s [3/2]₂ line. The first segment of the trace (left hand side) shows the signal levels recorded without the discharge. The levels for no lasers, the pump laser alone and the pump pulse probe lasers are indicated. The discharge was then turned on with the probe laser tuned off-resonance. Finally, the probe laser was scanned across the the 5p[1/2]₁-5s[3/2]₂ line, producing the gain feature that is evident near the center of the trace.

then turned on, resulting in a further slight increase of the baseline. Finally, gain was observed when the probe laser was scanned over the 5p[1/2]₁ - 5s[3/2]₂ line. When on- resonance, the probe laser was entirely absorbed when the pump laser was blocked or tuned off-resonance.

The population inversion achieved in the second experiment relied on rapid collisional energy transfer between the 5p[5/2]₃ and 5p[1/2]₁ levels. To explore the effect of the pressure on the inversion kinetics, gain measurements were performed for Kr (27 mbar) in He at total pressures ranging from 200-2000 mbar. Results from these measurements are presented in Fig. 11. For these experiments the pump and probe lasers were tuned to the 5p[5/2]₃-5s[3/2]₂ and 5p[1/2]₁-5s[3/2]₂ lines, respectively. The traces are time-resolved signals, with pre- probe pulse data that indicate undetectable light levels (on this sensitivity scale) from the discharge. Gain is apparent for pressures above 600 mbar. The gain increased with increasing pressure up to approximately 1400 mbar, reaching a plateau at higher pressures. This behavior is readily understood in terms of the competition between radiative and collisional relaxation of the 5p[5/2]₃ level.

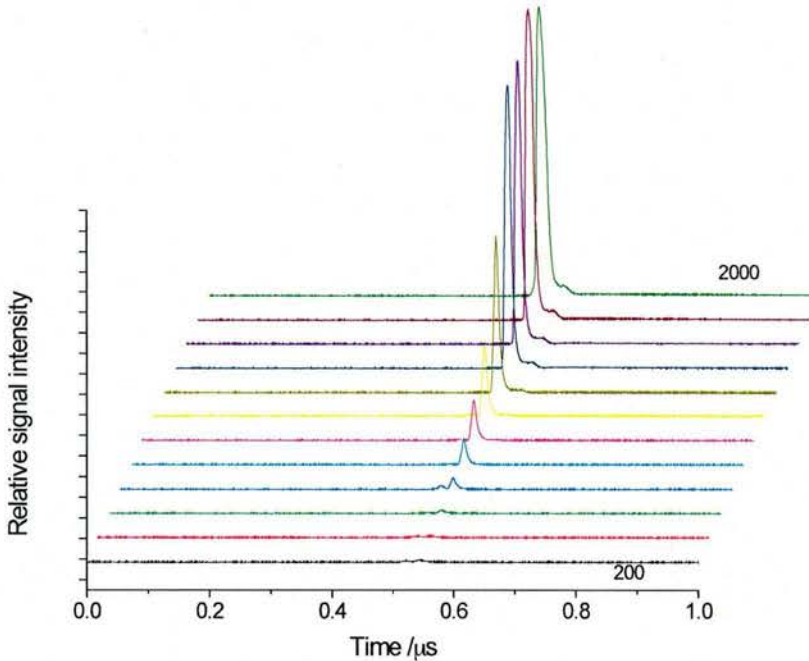


Figure 11. Dependence of the Kr* $5p[1/2]_1$ - $5s[3/2]_2$ gain on He pressure. These time-resolved traces were recorded for 27 mbar of Kr in He, with optical pumping of the $5p[5/2]_3$ - $5s[3/2]_2$ transition. Going from the lowest to the highest trace, the total pressures for these measurements were 200, 400, 600, 700, 800, 900, 1000, 1200, 1400, 1600, 1800 and 2000 mbar. The delay between the discharge and laser pulses was optimized for each pressure, within the range 5-25 μ s.

Lasing of the Kr*/He mixtures was observed when the rear window of the discharge cavity was replaced by a total reflector. The output, viewed using an IR phosphor card approximately 4 m away from the polarizer, was a well-defined beam. For 27 mbar of Kr in 973 mbar of He, the output was completely dominated by the $5p[1/2]_1 \rightarrow 5s[3/2]_2$ laser line. Pumping of higher energy levels of Kr $4p^5 5p$ manifold was also examined. As can be seen in Fig. 12, $5p[1/2]_1 \rightarrow 5s[3/2]_2$ gain was observed for excitation of the $5p[5/2]_2$, $5p[3/2]_1$ and $5p[3/2]_2$ levels.

Following these observations, preliminary experiments were conducted in order to test for optically pumped lasing of Ne*, Ar* and Xe*. For all three Rg/He mixtures (27 mbar Rg in 973 mbar He), excitation of $(n+1)p[5/2]_3$ yielded lasing on the $(n+1)p[1/2]_1 \rightarrow (n+1)s[3/2]_2$ transitions. The pump and lasing wavelengths were those given in Table 1. As Ar is an inexpensive reagent, we were able to investigate the effect of using high mole fractions in the gas mixture. It was found that lasing could be achieved using pure Ar at a pressure of 1000 mbar.

The laser performance characteristics of the Rg/He mixtures were all quite similar for Rg=Ne, Ar, Kr and Xe. Power measurements were made for Ar (27 mbar) in He (973 mbar). With a pump pulse energy of 0.26 mJ the lasing energy measured after the polarizer was 0.017 mJ. As

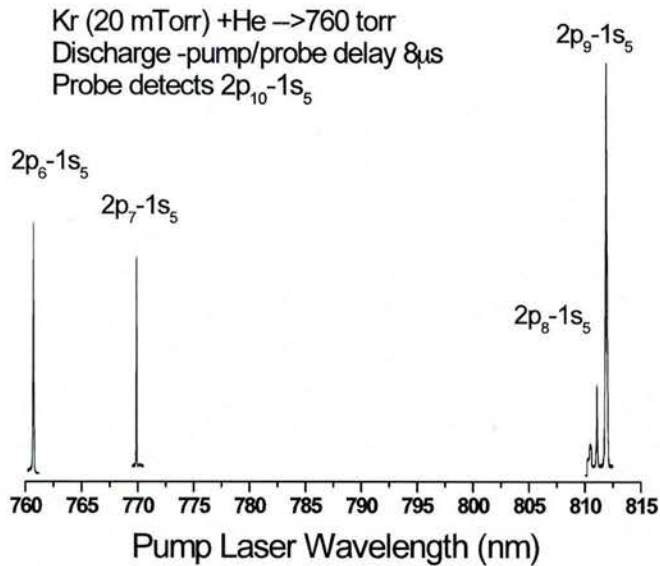


Figure 12. Gain on the Kr^* $5p[1/2]_1 - 5s[3/2]_2$ transition induced by excitation of the $5p[5/2]_3$, $5p[5/2]_2$, $5p[3/2]_1$ and $5p[3/2]_2$ states. The pump and probe lasers were fired 8 μs after the discharge pulse. The line intensities in this figure have not been corrected for wavelength dependent variations in the pump laser power.

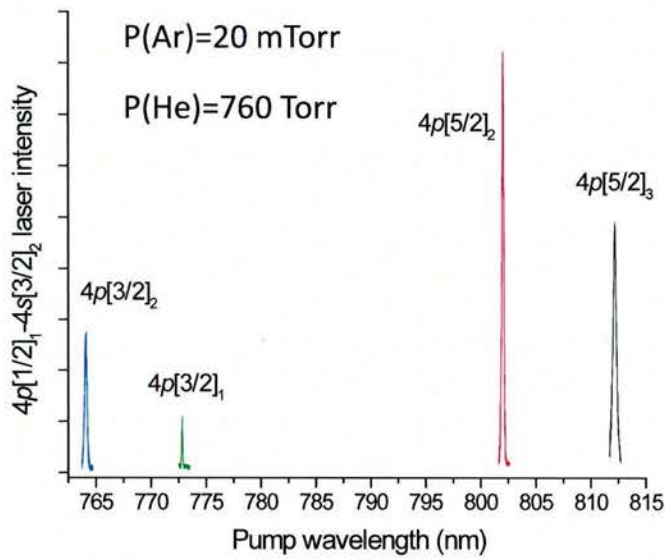


Figure 13. Lasing of Ar^* produced by four different pump wavelengths

the laser cavity did not include any polarizing elements, the output power would be twice this value (at least, as this estimate neglects the reflection and scattering losses of the polarizer). An

output energy of 0.034 mJ corresponds to a photon conversion efficiency (pump to lasing) of 13% and a peak output intensity of approximately 27 kW cm^{-2} .

Experiments with Ar*/He mixtures were extended by examining the effectiveness of pumping higher energy states of the $3p^54p$ manifold. Figure 13 shows the $4p[1/2]_1 \rightarrow 4s[3/2]_2$ lasing intensity for excitation of the $4p[5/2]_3$, $4p[5/2]_2$, $4p[3/2]_1$ and $4p[3/2]_2$ states. In all cases the population cascade back to $4p[1/2]_1$ was fast enough to result in lasing. As Ar is relatively inexpensive, we were able to explore the effect of substantially increasing the fraction of Ar in the gas mixture. Lasing was observed for all compositions, up to and including the limit of pure Ar. The latter observation was particularly surprising as efficient quenching of the $4p$ states by collisions with Ar had been reported for measurements conducted at low-pressure¹⁹.

5. CW diode laser pumping of an Ar* laser

Pulsed laser demonstrations established important milestones, and yielded valuable insights concerning the laser kinetics. However, the ultimate goal is the development of high-power CW laser systems. Consequently, it was a priority to test whether Rg* lasers can be driven using CW light sources. Demonstration experiments with CW lasers are generally more demanding as COTS systems cannot approach the peak intensities that are readily available from pulsed lasers. To enable the first experiments with CW pumping of an Rg* laser system, the group at the University of Central Florida (UCF) constructed a diode laser that was tailored for optical pumping of Ar* at 811.5 nm (described in Section A, 1.7). This device could be temperature tuned over a range of 3 cm^{-1} , had a linewidth of 0.3 cm^{-1} and a maximum output power of 7.5 W. For laser demonstration experiments using this pump source, the Ar* metastables were generated in a small glass discharge cell that was equipped with rectangular stainless steel discharge plates (2.5 cm long by 1 cm wide). The plates were separated by approximately 0.5 cm. A pulsed discharge of 1 μs duration was used to excite He/Ar gas mixtures at total pressures in the range of 0.1-1 atm. The optical configuration is shown in Fig.14, while time-resolved signals from this experiment are shown in Fig. 15. The upper trace of Fig. 15 shows the transient absorption of the pump laser achieved by a single pass through the discharge-excited gas. The lower trace shows the resulting Ar* laser pulse. Power dependence measurements indicated a threshold pump power of 3.5 W, and linear power scaling from 4-7.5 W. These measurements confirm that CW optical pumping of an Ar* laser can be accomplished using a modest power level.

Future work will be directed towards the development of continuous discharge sources for metastable production and studies of power scaling. The initial indications are that optically pumped rare gas lasers may offer the same desirable performance characteristics as DPAL's, without the chemical complexities.

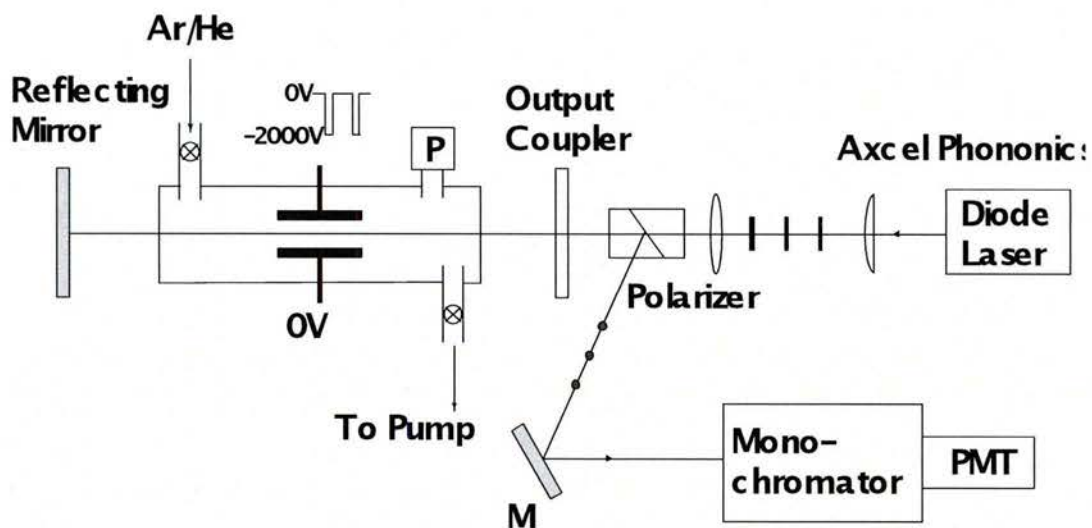


Figure 14. Optical configuration used for CW pumping of Ar*

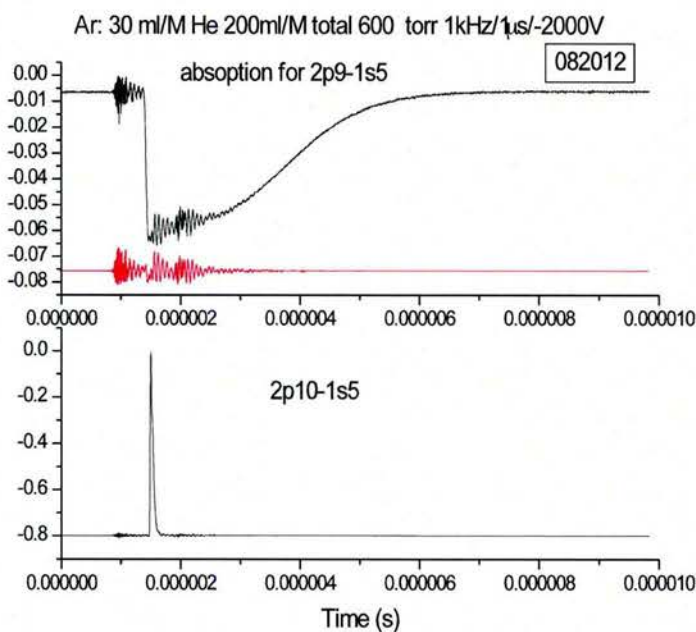


Figure 15. Time-resolved absorption and emission signals from the apparatus shown in Fig. 14.

References for Section B

- 1 W. F. Krupke, R. J. Beach, V. K. Kanz, and S. A. Payne, Optics Letters 28, 2336 (2003). "*Resonance transition 795-nm rubidium laser*"
- 2 R. J. Beach, W. F. Krupke, V. K. Kanz, S. A. Payne, M. A. Dubinskii, and L. D. Merkle, Journal of the Optical Society of America B: Optical Physics 21, 2151 (2004). "*End-pumped continuous-wave alkali vapor lasers: experiment, model, and power scaling*"
- 3 W. F. Krupke, R. J. Beach, V. K. Kanz, and S. A. Payne, Proceedings of SPIE-The International Society for Optical Engineering 5334, 156 (2004). "*DPAL: a new class of CW near-infrared high-power diode-pumped alkali (vapor) lasers*"
- 4 T. Ehrenreich, B. Zhdanov, T. Takekoshi, S. P. Phipps, and R. J. Knize, Electronics Letters 41, 415 (2005). "*Diode pumped cesium laser*"
- 5 B. V. Zhdanov, T. Ehrenreich, and R. J. Knize, Optics Communications 260, 696 (2006). "*Highly efficient optically pumped cesium vapor laser*"
- 6 T. A. Perschbacher, D. A. Hostutler, and T. M. Shay, Proceedings of SPIE-The International Society for Optical Engineering 6346, 634607/1 (2007). "*High-efficiency diode-pumped rubidium laser: experimental results*"
- 7 S. S. Q. Wu, T. F. Soules, R. H. Page, S. C. Mitchell, V. K. Kanz, and R. J. Beach, Optics Letters 32, 2423 (2007). "*Hydrocarbon-free resonance transition 795-nm rubidium laser*"
- 8 B. Zhdanov and R. J. Knize, Optics Letters 32, 2167 (2007). "*Diode-pumped 10 W continuous wave cesium laser*"
- 9 B. V. Zhdanov and R. J. Knize, Proceedings of SPIE 7022, 70220J/1 (2008). "*Advanced diode-pumped alkali lasers*"
- 10 B. V. Zhdanov, A. Stooke, G. Boyadjian, A. Voci, and R. J. Knize, Electronics Letters 44, 735 (2008). "*Optically pumped caesium-Freon laser*"
- 11 B. V. Zhdanov, M. K. Shaffer, and R. J. Knize, Optics Express 17, 14767 (2009). "*Cs laser with unstable cavity transversely pumped by multiple diode lasers*"
- 12 J. Zweiback, G. Hager, and W. F. Krupke, Optics Communications 282, 1871 (2009). "*High efficiency hydrocarbon-free resonance transition potassium laser*"
- 13 A. M. Komashko and J. Zweiback, Proceedings of SPIE 7581, 75810H/1 (2010). "*Modeling laser performance of scalable side pumped alkali laser*"
- 14 A. V. Bogachev, S. G. Garanin, A. M. Dudov, V. A. Yeroshenko, S. M. Kulikov, G. T. Mikaelian, V. A. Panarin, V. O. Pautov, A. V. Rus, and S. A. Sukharev, Quantum Electronics 42, 95 (2012). "*Diode-pumped cesium vapour laser with closed-cycle laser-active medium circulation*"
- 15 D. W. Setser, T. D. Dreiling, H. C. Brashears, Jr., and J. H. Kolts, Faraday Discussions of the Chemical Society 67, 255 (1979). "*Analogy between electronically excited state atoms and alkali metal atoms*"
- 16 D. H. Stedman and D. W. Setser, Progress in Reaction Kinetics 6, 193 (1971). "*Chemical applications of metastable rare gas atoms*"
- 17 NIST, (2012).
- 18 R. S. F. Chang, H. Horiguchi, and D. W. Setser, Journal of Chemical Physics 73, 778 (1980). "*Radiative lifetimes and two-body collisional deactivation rate constants in argon for atomic krypton ($4p^5 5p$) and atomic krypton ($4p^5 5p'$) states*"

- ¹⁹ R. S. F. Chang and D. W. Setser, Journal of Chemical Physics **69**, 3885 (1978). "*Radiative lifetimes and two-body deactivation rate constants for argon($3p^5, 4p$) and argon($3p^5, 4p'$) states*"
- ²⁰ G. Zikratov and D. W. Setser, Journal of Chemical Physics **104**, 2243 (1996). "*State-to-state rate constants for the collisional interaction of Xe($7p$), Xe($6p'$), and Kr($5p'$) atoms with He and Ar*"
- ²¹ D. A. Zayarnyi and I. V. Kholin, Quantum Electronics **33**, 474 (2003). "*Penning high-pressure lasers on the $3p - 3s$ transitions in neon emitting at 703 and 920 nm*"
- ²² M. H. Kabir and M. C. Heaven, J. Phys. Chem. A **115**, 9724 (2011). "*Energy Transfer Kinetics of the $np^5(n + 1)p$ Excited States of Ne and Kr*"
- ²³ R. S. F. Chang and D. W. Setser, Journal of Chemical Physics **72**, 4099 (1980). "*Radiative lifetimes and collisional deactivation rate constants of excited atomic neon($2p^5 3p$) states*"